Mechanics of Materials 136 (2019) 103065

Contents lists available at ScienceDirect

Mechanics of Materials

journal homepage: www.elsevier.com/locate/mechmat

Research paper

An implicit formulation of the elasto-plastic self-consistent polycrystal plasticity model and its implementation in implicit finite elements

Milovan Zecevic, Marko Knezevic*

Department of Mechanical Engineering, University of New Hampshire, Durham, NH 03824, USA

ARTICLE INFO

Keywords:
Polycrystalline material
Crystal plasticity
Numerical algorithms
Finite elements
Deep drawing

ABSTRACT

Elasto-plastic self-consistent (EPSC) polycrystal plasticity theory has been used extensively in understanding and predicting anisotropic thermo-mechanical response and underlying microstructure evolution of polycrystalline metals. This paper describes the first implicit formulation of the EPSC model and its implementation in implicit finite elements. To this end, a suitably defined system of non-linear equations at the single crystal level and that at the polycrystal level homogenizing the single crystal solutions in terms of the rotation-neutralized increments in Cauchy stress and strain are formulated and numerically solved. The implicit EPSC model is first validated using the original explicit EPSC model. Subsequently, the implicit EPSC model is coupled with implicit finite elements (FE) through the use of the user material subroutine in Abaqus. To facilitate the efficient coupling, a stress update algorithm is developed and the consistent tangent stiffness operator is analytically derived. Here, every FE integration point embeds the implicit EPSC constitutive law taking into account microstructure evolution and the directionality of deformation mechanisms acting at the single crystal level. The multi-level FE-EPSC model is benchmarked using the single crystal data for copper and then applied to simulate drawing of a cup from an AA6022-T4 sheet. The implementation and insights from these predictions are presented and discussed in this paper.

1. Introduction

Metallic materials undergoing shaping and forming operations experience large plastic strains as well as frequent unloading and reloading, which cause highly non-uniform spatial stress-strain fields (Hosford and Caddell, 2011; Poulin et al., 2019; Roemer et al., 2019; Wagoner et al., 2013; Zecevic et al., 2016c). It is well known that crystallographic slip accommodates most of the plastic strains, while inducing plastic anisotropy in the mechanical response by evolution of crystallographic texture and dislocation structure. Additionally, intra- and inter-granular mechanical fields develop playing an important role in the deformation process, especially during unloading and reloading (Bauschinger, 1886; Ghorbanpour et al., 2017; Gribbin et al., 2016; Knezevic et al., 2013a; Pavlina et al., 2015). Upon a strain path change, the material exhibits non-linear unloading (Wagoner et al., 2013) followed by a reduction in yield stress from that reached at the end of preloading. The phenomenon is referred to as the Bauschinger effect (BE) (Bauschinger, 1886). The hardening rate that follows with continuation of loading is also different from that during pre-loading (Hasegawa et al., 1975; Zang et al., 2013). These characteristics of material behavior are governed by the evolution of the underlying microstructure and crystallographic texture. Crystal plasticity constitutive theories are designed to capture the underlying physics governing such microstructure evolution and the associated anisotropic stress-strain response of polycrystalline metals.

Over the past several decades, a number of crystal plasticity based models have been developed. For example, these include upper bound Taylor-type models (Al-Harbi et al., 2010; Knezevic et al., 2009, 2008a, b; Taylor, 1938; Van Houtte, 1982) and mean-field self-consistent models (Knezevic et al., 2016b; Lebensohn and Tomé, 1993; Lebensohn et al., 2016; Turner and Tomé, 1994; Zecevic et al., 2019a). As standalone (SA) codes, these models simulate uniform deformation, while not accounting for the heterogeneities in the mechanical fields that develop across the sample as a consequence of complex geometry. In contrast, crystal plasticity finite element (CPFE) and crystal plasticity fast Fourier transform (CPFFT) models can calculate the spatially resolved mechanical fields over explicit grain structure in 3D (Anand, 2004; Ardeljan et al., 2014, 2017; Ardeljan and Knezevic, 2018; Ardeljan et al., 2015, 2016b; Barrett et al., 2018; Cheng et al., 2018; Jahedi et al., 2014; Kalidindi et al., 2006; Knezevic et al., 2014c; Lebensohn et al., 2012; Savage et al., 2017; Zecevic et al., 2015b). However, these spatial models are computationally intensive and are

---

* Corresponding author.
E-mail address: marko.knezevic@unh.edu (M. Knezevic).

https://doi.org/10.1016/j.mechmat.2019.103065
Received 26 August 2018; Received in revised form 23 April 2019; Accepted 23 May 2019

typically used for modeling a representative volume element of a given material rather than a forming process (Eghtesad et al., 2018a, c; Knezevic and Savage, 2014; Savage and Knezevic, 2015). As a compromise, the mean-field models have been integrated in finite elements to operate at FE integration points facilitating complex deformation paths (Ardeljan et al., 2016a; Kalidindi et al., 1992; Knezevic et al., 2016a, 2013b; Segurado et al., 2012; Zecevic et al., 2016a).

One of the mean-field formulations is the elasto-plastic self-consistent (EPSC) model (Turner and Tomé, 1994). It is desirable because it accounts for granular elasticity. The model has been shown capable of predicting residual stress fields, elastic lattice strains, non-linear unloading, the BE, and hardening rates along with texture and twinning for various metals in a number of studies (Neil et al., 2010; Nugmanov et al., 2018; Wollmershauser et al., 2012; Zecevic et al., 2015a, 2016b, 2019b). The strategy of embedding the EPSC model at the meso-scale level in an implicit FE analysis at the macro-level was described in (Zecevic et al., 2017) for continuum elements and in (Zecevic and Knezevic, 2017) for shell elements. The overall model was termed FE-EPSC. The tangent stiffness matrix (Jacobian) required for the coupling was derived analytically facilitating fast convergence towards stress equilibrium.

In EPSC, the integration scheme for the rate equations is explicit. Specifically, the single crystal stress and shearing rates as well as the single crystal tangent stiffness are evaluated at the beginning of the given time increment and, thus, the self-consistent homogenization for the macroscopic tangent stiffness is performed with crystal properties evaluated at the beginning of the time increment (Neil et al., 2010; Turner and Tomé, 1994). Due to the explicit integration, the magnitudes of strain and rotation increments are limited to rather small values. The original FE-EPSC incorporating the explicit EPSC model required a sub-stepping procedure for strain increments passed from Abaqus to ensure accuracy of simulations (Zecevic et al., 2017). Such small values of increments can lead to a significant increase in the computational time due to the need to solve many increments. Computational efficiency is particularly a concern for the FE-EPSC implementation. In any simulation of a forming operation on polycrystalline metals using FE-EPSC, the single crystal stress equations for a large number of constituent grains followed by the self-consistent homogenization need to be solved at every integration point in the FE mesh for every trial displacement field. The time involved in the calculations scales approximately linearly with the number of increments. Thus, the main motivation for the development of the implicit EPSC model is to enable the FE-EPSC model to facilitate the use of large strain increments and eventually utilize strain increments provided by Abaqus relaxing the need for any sub-stepping. In addition, the lack of convergence of fixed-point iterations for calculation of polycrystal tangent stiffness occasionally occurs in cases when the number of constituent crystals used is small (on the order of a hundred), which is again the case relevant for FE-EPSC, where we attempt to minimize the amount of state variables and computational time. FE-EPSC typically runs with a hundred or a few hundred weighted orientations at each integration point.

To improve the efficiency of the original explicit EPSC formulation, this paper describes an implicit formulation of the EPSC model and its implementation in implicit finite elements. To this end, a suitably defined system of non-linear equations, homogenizing the single crystal solutions in terms of the rotation-neutralized increments in Cauchy stress and strain, is created and solved using Newton's method. The implicit EPSC model is first validated using the original explicit EPSC model. Case studies demonstrate that the implicit implementation can take large strain and rotation increments. Subsequently, the implicit EPSC model is coupled with implicit finite elements using the user material subroutine in Abaqus. The consistent tangent stiffness operator is analytically derived to provide the so-called Jacobian for the FE residual iterations. To illustrate the potential of the coupled multi-level FE-EPSC model, a sheet metal forming process of deep drawing subjecting the material to a multi-axial deformation path is simulated. A cup is drawn of an Al alloy AA6022-T4 sheet. In addition to drawing, the subsequent springback unloading step is simulated. Here, granular elasticity, intra-granular backstresses, backstress aided dislocation glide, and inter-granular stresses are taken into account. Shell elements are used in the simulation as sheet metal forming simulations are typically performed using shell elements because of their computational efficiency. The FE-EPSC multi-level model developed in this work can be used as a simulation tool for simulating forming of anisotropic metals taking into account the effects of microstructure on the flow properties.

2. Constitutive relations

In the presence of large strains and rotations, a constitutive relation between the Jaumann rate of Cauchy stress, $\hat{\boldsymbol{\sigma}}$, and the average strain rate, $\dot{\boldsymbol{\varepsilon}}$, for a material point is (Nagtegaal and Veldpaus, 1984; Neil et al., 2010):

$$\hat{\boldsymbol{\sigma}} = \mathbf{L}\dot{\boldsymbol{\varepsilon}} = \dot{\boldsymbol{\sigma}} + \boldsymbol{\sigma}\mathbf{W} - \mathbf{W}\boldsymbol{\sigma}, \tag{1}$$

where $\mathbf{L}$ is the tangent stiffness, $\boldsymbol{\sigma}$ is the Cauchy stress, and $\mathbf{W}$ is the spin tensor. The relation holds for a material point, which could be thought as the representative volume element (RVE) of the material i.e. a minimum volume of the material such that the response from the volume is representative for the continuum (van Mier, 1997). The material point can be a single crystal or a polycrystalline point. While single crystals are usually assumed to be homogenous, polycrystalline materials are heterogeneous because they consist of single crystals, which introduces heterogeneities in the mechanical fields. Thus, defining constitutive relation for a polycrystalline material involves a homogenization of known responses of constituent single crystals. In what follows, a brief review of generally accepted relations describing constitutive response of polycrystalline metallic materials is given (Hutchinson, 1970; Kocks et al., 1998; Lipinski and Berveiller, 1989; Nagtegaal and Veldpaus, 1984; Neil et al., 2010; Schröder and Miehe, 1997; Turner and Tomé, 1994). In our description, "$\cdot$" and "$\otimes$" are used to denote a dot product and a tensor product, respectively.

2.1. Single crystal constitutive relation

Every single crystal occupies some volume in a polycrystal. During a deformation process, every point in this volume experiences motion. The strain rate and spin rate kinematic quantities are calculated from the motion. The quantities are assumed to be uniform within each single crystal and are denoted as $\dot{\boldsymbol{\varepsilon}}^c$ and $\mathbf{W}^c$, respectively. Since $\dot{\boldsymbol{\varepsilon}}^c$ and $\mathbf{W}^c$ are defined as symmetric and anti-symmetric parts of velocity gradient, respectively, they are expressed in the current configuration. All relations in this section are likewise written with respect to the current configuration.

Hooks law, in the rate form, for a crystal undergoing rigid body rotation, in the presence of plastic strain, is:

$$\hat{\boldsymbol{\sigma}}^c = \mathbf{C}^c(\dot{\boldsymbol{\varepsilon}}^c - \dot{\boldsymbol{\varepsilon}}^{pl,c}) - \boldsymbol{\sigma}^c tr(\dot{\boldsymbol{\varepsilon}}^c), \tag{2}$$

where $\hat{\boldsymbol{\sigma}}^c$ is the Jaumann rate of Cauchy stress, $\mathbf{C}^c$ is an elastic stiffness tensor of a single crystal, $\dot{\boldsymbol{\varepsilon}}^c$ is a total strain rate and $\dot{\boldsymbol{\varepsilon}}^{pl,c}$ is a plastic strain rate. The plastic strain rate inside a crystal is defined as:

$$\dot{\boldsymbol{\varepsilon}}^{pl,c} = \sum_s \mathbf{m}^s \dot{\gamma}^s, \tag{3}$$

where $\mathbf{m}^s = \frac{1}{2}(\mathbf{b}^s \otimes \mathbf{n}^s + \mathbf{n}^s \otimes \mathbf{b}^s)$ is the symmetric Schmid tensor, defined by $\mathbf{b}^s$, which is the slip system Burgers vector in the current configuration and $\mathbf{n}^s$, which is the slip system normal vector in the current configuration. $\dot{\gamma}^s$ is a shear rate on the slip system s. The sum is over all active slip systems. Slip systems are active if they fulfill the following conditions:

$$\boldsymbol{\sigma}^{c}\cdot\mathbf{m}^{s} = \tau_{c}^{s}, \tag{4a}$$

$$\overset{\wedge}{\boldsymbol{\sigma}}{}^{c}\cdot\mathbf{m}^{s} = \dot{\tau}_{c}^{s}, \tag{4b}$$

where τ_c^s is the slip resistance of a slip system s. The values of slip resistance per s define the single crystal yield surface. The single crystal yield surface consists of multiple hyper-planes in stress space, corresponding to individual slip systems (Knockaert et al., 2000). The first condition means that for a slip system to be active, the stress state needs to be on the yield surface i.e. hyper-plane in the stress space corresponding to the slip system, while the second condition is the consistency condition, which ensures that the stress state remains on the yield surface. The yield surface evolves due to strain hardening. The evolution of slip resistance is coupled with shearing rates using:

$$\dot{\tau}_{c}^{s} = \sum_{s'} h^{ss'}\dot{\gamma}^{s'}, \tag{5}$$

where $h^{ss'}$ is the hardening matrix. It is assumed that the evolution of slip resistance is a known function of shear strain, $\tau_c^s(\gamma^{s'})$. As a result, the hardening matrix is a matrix of partial derivatives $h^{ss'} = \frac{\partial \tau_c^s}{\partial \gamma^{s'}}(\gamma^{s''})$. Specific expressions for the evolution of slip resistance and the hardening matrix are described later. Following Eq. (1), the single crystal constitutive relation is:

$$\overset{\wedge}{\boldsymbol{\sigma}}{}^{c} = \mathbf{L}^{c}\dot{\boldsymbol{\varepsilon}}^{c}. \tag{6}$$

In Eq. (6), $\mathbf{L}^c$ is the elasto-plastic instantaneous stiffness tensor (or the tangent stiffness) and is given by (Neil et al., 2010):

$$\mathbf{L}^{c} = \mathbf{C}^{c} - \mathbf{C}^{c}\sum_{s}\mathbf{m}^{s}\otimes\left(\sum_{s'}\left(X^{ss'}\right)^{-1}\mathbf{m}^{s'}(\mathbf{C}^{c} - \boldsymbol{\sigma}^{c}\otimes\ \mathbf{i})\right) - \boldsymbol{\sigma}^{c}\otimes\ \mathbf{i}, \tag{7}$$

with:

$$X^{ss'} = h^{ss'} + \mathbf{C}^{c}\cdot\mathbf{m}^{s}\otimes\ \mathbf{m}^{s'}, \tag{8}$$

where $\mathbf{i}$ is the second rank identity tensor, and indices s and s' span over all active slip systems in a grain c. The tangent stiffness in the elasto-plastic deformation regime has the same meaning as the elastic stiffness in the elastic deformation regime, with that it applies to the rates of stress and strain and not the total quantities, and therefore can be referred to as the property of a single crystal.

It remains to define the crystal rigid body rotation for crystal re-orientation i.e. texture evolution. The elastic spin rate of a crystal c is:

$$\mathbf{W}^{c} = \mathbf{W}^{c,app} - \mathbf{W}^{pl,c}, \tag{9}$$

where $\mathbf{W}^{c,\ app}$ is a total applied spin and $\mathbf{W}^{pl,\ c}$ is a plastic spin. This total applied spin is a sum of an overall applied macroscopic spin, $\mathbf{W}$, and a spin originating from the antisymmetric Eshelby tensor for crystal c, $\boldsymbol{\Pi}^c$, which will be defined shortly. The plastic spin is:

$$\mathbf{W}^{pl,c} = \sum_{s}\dot{\gamma}^{s}\mathbf{q}^{s}, \tag{10}$$

where $\mathbf{q}^{s} = \frac{1}{2}(\mathbf{b}^{s}\otimes\ \mathbf{n}^{s} - \mathbf{n}^{s}\otimes\ \mathbf{b}^{s})$ is the antisymmetric Schmid tensor.

2.2. Polycrystalline constitutive relation

The polycrystalline constitutive relation used in the present work is that of the EPSC model (Zecevic and Knezevic, 2018). This model relates the deformation of each crystal to the deformation of the polycrystal using the self-consistent homogenization scheme (Neil et al., 2010; Turner and Tomé, 1994). The polycrystal is represented by a collection of single crystals each having a specific crystal lattice orientation, an ellipsoidal shape, and a volume fraction. The mechanical fields of each crystal are determined by considering each crystal as an elasto-plastic inclusion in the homogeneous effective medium (HEM). The HEM has properties of the polycrystal, which is assumed to be an RVE of a material.

Homogeneous boundary conditions are treatable by a standalone EPSC (SA-EPSC) model. For example, we can impose strain increments ($\dot{\boldsymbol{\varepsilon}}\Delta t$) along the loading direction, while enforcing zero average stress along the two lateral directions of the sample to simulate simple tension/compression. An applied deformation can consist of an applied spin, $\mathbf{W}$, like in simple shear deformation. In contrast to SA-EPSC, FE-EPSC can handle any boundary conditions facilitated by the FE framework, as will be described later.

Following Eq. (1), the linear constitutive relation between the Jaumann rate of Cauchy stress and the strain rate for a polycrystal is:

$$\overset{\wedge}{\boldsymbol{\sigma}} = \mathbf{L}\dot{\boldsymbol{\varepsilon}} \tag{11}$$

where $\overset{\wedge}{\boldsymbol{\sigma}}$is the overall Jaumann rate, $\dot{\boldsymbol{\varepsilon}}$ is the overall strain rate, and $\mathbf{L}$ is the tangent stiffness of HEM i.e. the polycrystal. The HEM tangent stiffness is defined based on the self-consistent homogenization approach. The unknown tangent stiffness of the HEM can be determined by enforcing:

$$\overset{\wedge}{\boldsymbol{\sigma}} = \langle\overset{\wedge}{\boldsymbol{\sigma}}{}^{c}\rangle, \tag{12}$$

$$\dot{\boldsymbol{\varepsilon}} = \langle\dot{\boldsymbol{\varepsilon}}^{c}\rangle, \tag{13}$$

where $\langle\,\rangle$ indicate volume average over single crystal quantities, c. The above relations result in an implicit equation for the HEM tangent stiffness:

$$\mathbf{L} = \langle\mathbf{L}^{c}\mathbf{A}^{c}\rangle\langle\mathbf{A}^{c}\rangle^{-1}, \tag{14}$$

with:

$$\mathbf{A}^{c} = (\mathbf{L}^{c} + \mathbf{L}^{*})^{-1}(\mathbf{L} + \mathbf{L}^{*}), \tag{15}$$

$$\mathbf{L}^{*} = \mathbf{L}(\mathbf{S}^{c-1} - \mathbf{I}), \tag{16}$$

where $\mathbf{L}$, $\mathbf{L}^c$, $\mathbf{L}^*$ and $\mathbf{S}^c$ are the macroscopic tangent stiffness, the crystal tangent stiffness, an interaction tensor, and the symmetric portion of the Eshelby tensor, respectively.

From the Eshelby solution of a single crystal inhomogeneity inside HEM and applied boundary conditions, an additional spin per crystal is calculated as:

$$\boldsymbol{\Pi}^{c} = \mathbf{P}^{c}(\mathbf{S}^{c})^{-1}(\dot{\boldsymbol{\varepsilon}}^{c} - \dot{\boldsymbol{\varepsilon}}), \tag{17}$$

where $\mathbf{P}^c$ is the antisymmetric Eshelby tensor and $\boldsymbol{\Pi}^c$ is the calculated spin.

3. Implicit integration of the rate equations in EPSC

The rate equations presented in Section 2 describe a continuum problem in the current configuration. Imposed strain rate, $\dot{\boldsymbol{\varepsilon}}$, and spin rate, $\mathbf{W}$, to a polycrystal are known. These constitute an applied strain history. The objective is to find the stress history using an integration algorithm (Simo and Taylor, 1985). The converged solution at time t is known and the integration is performed over a time increment Δt. The imposed deformation, $\dot{\boldsymbol{\varepsilon}}$, and the rigid body rotation, $\mathbf{W}$, can be treated separately (Abaqus, 2012). The decoupling allows separate treatment of any imposed rigid body rotation by simply rotating all tensors with an incremental rotation matrix, $\Delta\mathbf{R}$, which corresponds to $\mathbf{W}$. Therefore, the macroscopic spin is not explicitly needed for the integration procedure and, thus, is not considered to act in the rate equations presented in Section 2. The single crystal constitutive equation, Eq. (2), is integrated to incremental form (Nagtegaal and Veldpaus, 1984). The integration requires a choice of a fixed configuration in which variables are expressed and integrated. Likewise, the polycrystal constitutive equation needs to be expressed in an incremental form at a fixed configuration. Once the equations are in the incremental form, in a given configuration, the problem can be formulated as a set of non-linear equations. As a result, the continuum model is replaced with a non-linear incremental model (Simo and Taylor, 1985). Several steps are specifically identified in the integration algorithm developed in the present work: (a) decoupling deformation and rotation, (b) integrating the single crystal constitutive relation, and (c) solving a system of non-linear equations for a polycrystal in an incremental form.

It is worth mentioning that the integration of a single crystal response can be treated independently from the polycrystal homogenization procedure (Zeng et al., 2015). Several single crystal algorithms have been proposed in literature (Anand and Kothari, 1996; Ben Bettaieb et al., 2012; Horstemeyer et al., 2005; Knockaert et al., 2000; Schröder and Miehe, 1997). The integration algorithm followed in the present work was proposed as explicit in Knockaert et al. (2000), but first introduced in Borja and Wren (1993). The algorithm was further developed as implicit in Ben Bettaieb et al. (2012). The algorithm is particularly suitable for the present development because it solves for the time increment over which there is no change in active slip systems, with the known set of active slip systems at the start of the increment. On the other hand, other evaluated algorithms use fixed time increment and search for the unknown set of active slip systems. This results in a situation that a set of active slip systems is essentially enforced to be active during the whole time increment, creating a strong constraint which cannot always be successfully satisfied, especially if time increments are large. The solution procedure for the system of non-linear equations at a polycrystal level follows the procedure developed for the visco-plastic self-consistent (VPSC) model in Lebensohn and Tomé (1993), with some adjustment.

3.1. Decoupling deformation and rotation effects at a single crystal level

Generally, a crystal is simultaneously subjected to a strain rate, $\dot{\boldsymbol{\varepsilon}}^c$, and a spin rate, $\mathbf{W}^c$. Even though the macroscopic spin is not considered, there are still the plastic spin, $\mathbf{W}^{pl,\ c}$, and the spin from anti-symmetric Eshelby tensor, $\boldsymbol{\Pi}^c$, contributing to $\mathbf{W}^c$. We distinguish three configurations: the initial configuration for the current increment at t, the current configuration at τ ($t < \tau < t + \Delta t$), and the configuration at the end of the current increment $t + \Delta t$. Fig. 1 shows the configuration at t and the configuration at $t + \Delta t$ for a crystal with respect to the sample frame. We remind that the continuum rate equations presented in Section 2 are intrinsically expressed in the current configuration, τ.

Integration of a tensor must be performed in one configuration, since addition of tensors defined in different configurations is not meaningful. Therefore, one configuration needs to be chosen and all tensors should be rotated to this configuration before integration. We choose the known configuration at t to express all tensor quantities (Nagtegaal and Veldpaus, 1984). The rotation tensor that rotates vectors from the configuration at t to the current configuration at τ is:

$$\mathbf{n}^c = \Delta\mathbf{R}^c(\tau)\ \bar{\mathbf{n}}^c, \tag{18}$$

where $\bar{\mathbf{n}}^c$ is a vector in the configuration at t, $\mathbf{n}^c$ is a vector in the configuration at τ and $\Delta\mathbf{R}^c(\tau)$ is an incremental active rotation matrix calculated from the spin, $\mathbf{W}^c$. Next, we can rotate all essential quantities to the configuration at t using (Nagtegaal and Veldpaus, 1984):

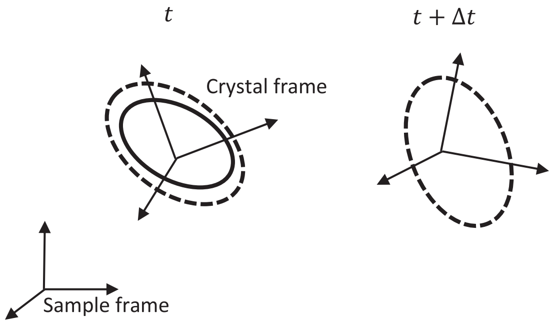

Fig. 1. Configurations at t and $t + \Delta t$ showing decoupling of deformation, $\dot{\boldsymbol{\varepsilon}}^c$, and rotation corresponding to $\mathbf{W}^c$.

$$\begin{aligned}&\bar{\boldsymbol{\sigma}}^c = \Delta\mathbf{R}^{cT}(\tau)\boldsymbol{\sigma}^c\Delta\mathbf{R}^c(\tau);\ \dot{\bar{\boldsymbol{\sigma}}}^c = \Delta\mathbf{R}^{cT}(\tau)\overset{\triangle}{\boldsymbol{\sigma}}{}^c\Delta\mathbf{R}^c(\tau);\\ &\bar{\mathbf{W}}^c = \Delta\mathbf{R}^{cT}(\tau)\mathbf{W}^c\Delta\mathbf{R}^c(\tau);\dot{\bar{\boldsymbol{\varepsilon}}}^c = \Delta\mathbf{R}^{cT}(\tau)\dot{\boldsymbol{\varepsilon}}^c\Delta\mathbf{R}^c(\tau);\ \bar{L}_{ijkl}\\ &\quad = \Delta R_{pi}(\tau)\Delta R_{qj}(\tau)\Delta R_{rk}(\tau)\Delta R_{sl}(\tau)L_{pqrs}.\end{aligned} \tag{19}$$

Quantities expressed in the configuration at t are called the rotation-neutralized quantities and are denoted with the bar on top of them. The constitutive relation expressed in terms of the rotation-neutralized quantities is:

$$\dot{\bar{\boldsymbol{\sigma}}}^c = \bar{\mathbf{L}}^c\dot{\bar{\boldsymbol{\varepsilon}}}^c,\quad \text{with the initial condition of}\ \bar{\boldsymbol{\sigma}}^c(t) = \bar{\boldsymbol{\sigma}}^c_t. \tag{20}$$

If we integrate the Eq. (20), we obtain the increment in stress (Nagtegaal and Veldpaus, 1984):

$$\Delta\bar{\boldsymbol{\sigma}}^c = \int_t^{t+\Delta t}\bar{\mathbf{L}}^c\dot{\bar{\boldsymbol{\varepsilon}}}^c dt = \frac{1}{\Delta t}\left(\int_t^{t+\Delta t}\bar{\mathbf{L}}^c dt\right)\Delta\bar{\boldsymbol{\varepsilon}}^c, \tag{21}$$

where $\dot{\bar{\boldsymbol{\varepsilon}}}^c = \frac{\Delta\bar{\boldsymbol{\varepsilon}}^c}{\Delta t} = const$. This amounts to applying the deformation defined with $\Delta\bar{\boldsymbol{\varepsilon}}^c$, followed by the rotation $\Delta\mathbf{R}^c_{t+\Delta t} = \Delta\mathbf{R}^c(\tau = t + \Delta t)$ of all tensors to configuration at $t + \Delta t$, as shown in Fig. 1. For instance, the stress is updated using:

$$\boldsymbol{\sigma}^c_{t+\Delta t} = \Delta\mathbf{R}^c_{t+\Delta t}(\bar{\boldsymbol{\sigma}}^c_t + \Delta\bar{\boldsymbol{\sigma}}^c)\Delta\mathbf{R}^c_{t+\Delta t}{}^T. \tag{22}$$

3.2. Integration of the single crystal constitutive relation in its incremental form

The incremental form of the constitutive law for a single crystal is:

$$\Delta\bar{\boldsymbol{\sigma}}^c = \bar{\mathbf{L}}^{inc,c}\Delta\bar{\boldsymbol{\varepsilon}}^c, \tag{23}$$

where $\bar{\mathbf{L}}^{inc,c} = \frac{1}{\Delta t}\int\limits_t^{t+\Delta t}\bar{\mathbf{L}}^c dt$ is the tangent stiffness relating the increments in strain and Cauchy stress. We conveniently introduce the new variable, $\bar{\mathbf{L}}^{inc,c}$, for the integral of $\bar{\mathbf{L}}^c$ since the latter might be evaluated multiple times within the increment. Examination of the expression for tangent stiffness (7) and (8) shows the dependence:

$$\bar{\mathbf{L}}^c = \bar{\mathbf{L}}^c\left(A, \bar{\boldsymbol{\sigma}}^c, h^{ss'}\right),\ \text{with}\ s, s' \in A\left(\bar{\boldsymbol{\sigma}}^c, h^{ss'}, \tau^s, \dot{\bar{\boldsymbol{\varepsilon}}}^c\right), \tag{24}$$

where A is a set of active slip systems and s and s' go over active slip systems belonging to A. It is important to note that the set of active slip systems is determined based on the activation conditions (4a and b). Note also that for all active slip systems the condition, $\dot{\gamma}^s > 0$, must be fulfilled.

We point out that sub-discretization of a time increment Δt is a characteristic of our integration scheme. As a result, Δt can be reduced to Δt_{sub} in two ways. First, the sub-increment, Δt_{sub}, can be specified as an input and used throughout a simulation. This is beneficial for crystals with rapidly changing rate of hardening. Second, Δt can be reduced to Δt_{sub} by the integration procedure. Here, the sub-increment, Δt_{sub}, is treated as an unknown in the integration procedure. A vector representing the current stress in stress space can exit the yield surface if a constant increment size is used, since the stress is assumed to be on one set of hyper-planes in stress space. Moreover, if the stress vector at time t is within the single crystal yield surface, the response is assumed to be elastic during the increment, regardless weather the updated stress at $t + \Delta t$ is out of the yield surface. We develop a procedure to calculate the time increment over which the set of hyper-planes in contact with stress vector do not change. In other words, we calculate the portion of the increment over which the set of active slip systems does not change, ensuring that stress does not exit the single crystal yield surface. If sub-discretization is not set up as the input, the rule is that the integration algorithm updates variables from the start of the increment, t, to the end of the increment $t + \Delta t$. The exception is if the sub-discretization of the time increment is triggered then t_{sub} is initialized to t and then updated incrementally for Δt_{sub} until the end of the increment $t + \Delta t$. The sub-increment, Δt_{sub}, is often calculated in the elasto-plastic transition and in any strain path change portion of deformation but rarely

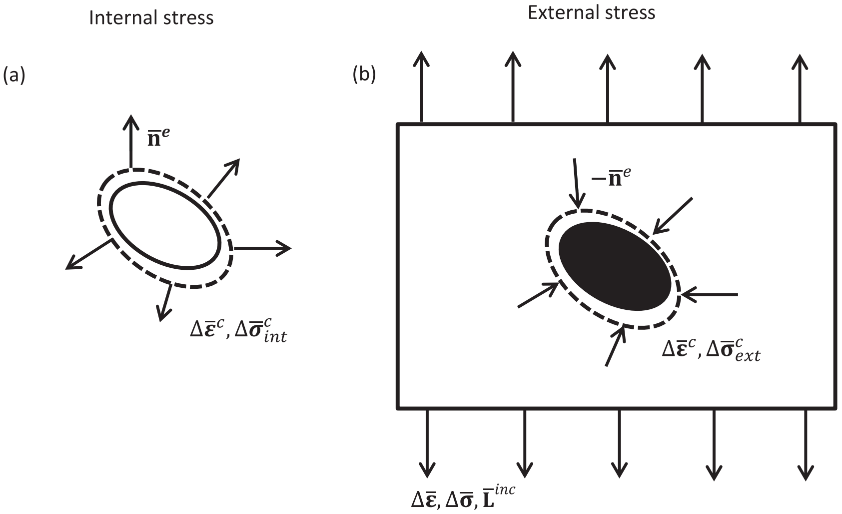

Fig. 2. Schematic showing the definition of the residual in terms of: (a) internal and (b) external stress increment.

otherwise.

We formulate an implicit solution procedure for shear rates facilitating large time increments. Using Eqs. (2), (4b), (3) and (5) written at the mid instant, i.e. $t + \frac{\Delta t}{2} = t_m$, we get:

$$\left(\bar{\mathbf{C}}^c\dot{\bar{\boldsymbol{\varepsilon}}}^c - \bar{\boldsymbol{\sigma}}^c_{t_m} tr\left(\dot{\bar{\boldsymbol{\varepsilon}}}^c\right)\right)\cdot\bar{\mathbf{m}}^s = \sum_{s'}\left(h^{ss'}_{t_m} + \bar{\mathbf{C}}^c\cdot\bar{\mathbf{m}}^{s'}\otimes\ \bar{\mathbf{m}}^s\right)\dot{\gamma}^{s'}_{t_m}, \tag{25}$$

with $\dot{\bar{\boldsymbol{\varepsilon}}}^c = \frac{\Delta\bar{\boldsymbol{\varepsilon}}^c}{\Delta t}$ and $\dot{\gamma}^{s'}_t = \frac{\Delta\gamma^{s'}}{\Delta t}$. Now, Eq. (25) represents a system of non-linear equations in terms of $\dot{\gamma}^{s'}_{t_m}$, since the hardening matrix, $h^{ss'}_{t_m}$, and the stress, $\bar{\boldsymbol{\sigma}}^c_{t_m}$, depend on shear rates. Since Eq. (25) is satisfied at an instant of time after t, the integration is implicit.

As always, the stress state at the end of the increment needs to be on or within the single crystal yield surface. The condition is enforced with Eq. (25) for all active slip systems. If the condition is violated for any of the inactive slip systems, meaning they become active during the increment, the increment Δt is adjusted so that only one of the inactive slip systems satisfies (Knockaert et al., 2000):

$$\bar{\boldsymbol{\sigma}}^c_{t+\Delta t}\cdot\bar{\mathbf{m}}^s = \tau^s_{c,t+\Delta t}. \tag{26}$$

As a result, the increment is reduced to the maximum value before activating the additional slip system, while the stress remains on the crystal yield surface. Eq. (26) is an additional relation to the system in Eq. (25) formulated to calculate Δt_{sub} (Ben Bettaieb et al., 2012; Knockaert et al., 2000) as:

$$\Delta t_{sub} = \min\frac{\tau^s_t - \bar{\boldsymbol{\sigma}}_{c,t}\cdot\bar{\mathbf{m}}^s}{\dot{\bar{\boldsymbol{\sigma}}}^c_{t_m}\cdot\bar{\mathbf{m}}^s - \sum_{s'} h^{ss'}_{t_m}\dot{\gamma}^{s'}_{t_m}}, \tag{27}$$

where min takes the minimum calculated value out of all inactive slip systems. Analogues to t_m, the mid instant becomes $t_{sub,m} = t_{sub} + \frac{\Delta t_{sub}}{2}$. We use the fixed point iteration scheme to solve the formulated system of non-linear equations for shear rates, $\dot{\gamma}^s$, and Δt_{sub}. Note that if there is no activation of any new slip systems within the increment then the solution for Δt_{sub} is Δt.

Next, $\bar{\mathbf{L}}^{inc,c}$ can be calculated. If the sub-incremental procedure is triggered then, $\bar{\mathbf{L}}^c$ is evaluated at multiple instances, k, during the total time increment, Δt. Here, the incremental tangent stiffness is a sum of those at the instances, k:

$$\bar{\mathbf{L}}^{inc,c} = \frac{1}{\Delta t}\int_{t+\Delta t}^{t}\bar{\mathbf{L}}^c dt = \frac{1}{\Delta t}\sum_k \bar{\mathbf{L}}^c_{t^k_{sub,m}}\Delta t^k_{sub,m}. \tag{28}$$

Note that the incremental tangent stiffness, $\bar{\mathbf{L}}^{inc,c}$, is evaluated with, $\bar{\mathbf{L}}^c_{t^k_{sub,m}}$, at τ $(t < \tau < t + \Delta t)$, and not from t. The subsequently calculated polycrystal tangent stiffness, $\bar{\mathbf{L}}^{inc}$, will contain information at τ $(t < \tau < t + \Delta t)$, making the overall procedure implicit.

Finally, the incremental plastic spin is evaluated using Eq. (10) as:

$$\bar{\mathbf{W}}^{pl,c}\Delta t = \sum_k \bar{\mathbf{W}}^{pl,c}_{t^k_{sub,m}}\Delta t^k_{sub,m} = \sum_k\sum_s \dot{\gamma}^s_{t^k_{sub,m}}\bar{\mathbf{q}}^s\Delta t^k_{sub,m}. \tag{29}$$

3.3. Solution procedure for a system of non-linear equations at the polycrystal level in an incremental form

The polycrystal incremental form of the constitutive law is obtained by performing the self-consistent homogenization of the incremental single crystal constitutive law solutions. This amounts to replacing the Jaumann rate of Cauchy stress and strain rate with the rotation-neutralized increment in Cauchy stress and the rotation-neutralized increment in strain, respectively. The term rotation-neutralized quantities at the polycrystal level is used to denote that the rotation-neutralized quantities at the single crystal level are used in deriving the macroscopic response. The macroscopic response is:

$$\Delta\bar{\boldsymbol{\sigma}} = \bar{\mathbf{L}}^{inc}\Delta\bar{\boldsymbol{\varepsilon}}, \tag{30}$$

where $\bar{\mathbf{L}}^{inc}$ is the HEM tangent stiffness, (Eq. (14)).

Replacing the rate form of the single crystal constitutive relation (Eq. (6)) and the polycrystal constitutive relation (Eq. (11)) in the homogenization procedure with their incremental forms (i.e. Eqs. (23) and (30)), produces a system of non-linear equations. The unknown variable in the system is the crystal strain increment $\Delta\bar{\boldsymbol{\varepsilon}}^c$, since the proposed algorithm for single crystal integration is strain driven.

Next, we suitably define a residual in terms of $\Delta\bar{\boldsymbol{\varepsilon}}^c$. For an initial guess of the $\Delta\bar{\boldsymbol{\varepsilon}}^c$ field, the single crystal integration can be performed to obtain an increment in stress $\Delta\bar{\boldsymbol{\sigma}}^c_{int} = \bar{\mathbf{L}}^{inc,c}\Delta\bar{\boldsymbol{\varepsilon}}^c$ and the tangent stiffness $\bar{\mathbf{L}}^{inc,c}$. This is depicted in Fig. 2a, where a crystal is shown independently, outside of the matrix, under the strain increment $\Delta\bar{\boldsymbol{\varepsilon}}^c$. The calculated stress increment, $\Delta\bar{\boldsymbol{\sigma}}^c_{int}$, defines the traction acting on the surface of the ellipsoid. Based on the calculated tangent stiffness, $\bar{\mathbf{L}}^{inc,c}$, the overall stiffness of polycrystal, $\bar{\mathbf{L}}^{inc}$, can be calculated using Eq. (14). Next, we consider the matrix having the tangent stiffness of the HEM, $\bar{\mathbf{L}}^{inc}$, from which the crystal c was removed to apply the strain increment, $\Delta\bar{\boldsymbol{\varepsilon}}^c$, to it (Fig. 2b). Now, the matrix has a cavity undergoing the increment in strain, $\Delta\bar{\boldsymbol{\varepsilon}}^c$, which is needed to fit the inhomogeneity back in it. The matrix has a certain displacement increment applied at its boundary giving rise to the strain and stress increments. The traction on the surface of the cavity, needed to produce the strain increment, $\Delta\bar{\boldsymbol{\varepsilon}}^c$, can be calculated from the interaction equation:

$$\Delta\bar{\boldsymbol{\sigma}}^c_{ext} = \Delta\bar{\boldsymbol{\sigma}} - \bar{\mathbf{L}}^*(\Delta\bar{\boldsymbol{\varepsilon}}^c - \Delta\bar{\boldsymbol{\varepsilon}}), \tag{31}$$

where $\Delta\bar{\boldsymbol{\sigma}}^c_{ext}$ is the external stress increment. In order to satisfy the equilibrium when the inclusion is placed back inside the matrix, the external and internal tractions must to be in balance, leading to:

$$\mathbf{r}(\Delta\bar{\boldsymbol{\varepsilon}}^c) = \Delta\bar{\boldsymbol{\sigma}}^c_{ext} - \Delta\bar{\boldsymbol{\sigma}}^c_{int} = \Delta\bar{\boldsymbol{\sigma}} - \bar{\mathbf{L}}^{*}(\Delta\bar{\boldsymbol{\varepsilon}}^c - \Delta\bar{\boldsymbol{\varepsilon}}) - \bar{\mathbf{L}}^{inc,c}\Delta\bar{\boldsymbol{\varepsilon}}^c. \tag{32}$$

The residual indicates how well the interaction equation is satisfied. As mentioned earlier, the definition of the residual along with the solution procedure were inspired by the algorithm present in VPSC (Lebensohn and Tomé, 1993). In VPSC, the fixed point iterations are used for the evaluation of crystal stress deviator. For each iteration, an appropriate interaction equation, analogues to Eq. (32), is solved in order to produce a new guess for crystal stress.

Finally, Newton's method is used to obtain the solution $\Delta\bar{\boldsymbol{\varepsilon}}^c$ by minimizing the residual. The Jacobian needed for Newton's method is defined as:

$$\mathbf{J}^c = \frac{\partial\mathbf{r}(\Delta\bar{\boldsymbol{\varepsilon}}^c)}{\partial\Delta\bar{\boldsymbol{\varepsilon}}^c} \cong -\bar{\mathbf{L}}^{*} - \bar{\mathbf{L}}^{inc,c}. \tag{33}$$

To test for convergence, the volume average of residuals for all grains is calculated and compared against the tolerance, i.e.:

$$\frac{10^k\langle\mathbf{r}(\Delta\bar{\boldsymbol{\varepsilon}}^c)\rangle}{\|\Delta\bar{\boldsymbol{\sigma}}\|_{tavg}} < 0.005. \tag{34}$$

with:

$$\|\Delta\bar{\boldsymbol{\sigma}}\|_{tavg} = \frac{\sum_{i=1}^{n_{inc}}\|\Delta\bar{\boldsymbol{\sigma}}^i\|\Delta t^i}{t} \tag{35}$$

where n_{inc} is the number of time increments applied by the time t i.e. $t = \sum_{i=1}^{n_{inc}}\Delta t^i$ and $k \geq 0$ is the smallest integer fulfilling the condition $0.1 < \|\Delta\bar{\boldsymbol{\sigma}}\|_{tavg}/(10^k\|\Delta\bar{\boldsymbol{\sigma}}\|) < 10$. If convergence is not achieved within predefined number of iterations the full Newton step is sequentially decreased with factors of 0.5, 0.2 and 0.1. If the condition (34) is still not satisfied after decreasing the Newton step, the applied increment in strain is applied within 4 steps, while the exponent k in the convergence criteria (34) is not reevaluated. The same procedure is used if one of the sub-increments is not converging. The cutting of strain increment and normalization of residual are inspired by the procedures used in Abaqus (2012). Once the criterion in Eq. (34) is fulfilled for the total imposed strain increment or all sub-increments, crystal spin, $\bar{\mathbf{W}}^c\Delta t$, can be updated and the corresponding rotation matrices, $\Delta\mathbf{R}^c_{t+\Delta t}$, can be calculated. The plastic spin was calculated during integration of the single crystal constitutive law in Section 3.1 (Eq. (28)). Since the macroscopic spin is not present, the only remaining spin is coming from the deviation of the single crystal strain rate from the applied macroscopic strain rate, due to treatment of single crystals as ellipsoidal inclusions in an infinite medium. This contribution to the total crystal spin is described by Eq. (17). The total incremental elastic spin is:

$$\bar{\mathbf{W}}^c\Delta t = \bar{\boldsymbol{\Pi}}^c\Delta t - \bar{\mathbf{W}}^{pl,c}\Delta t \tag{36}$$

The incremental rotation matrix for single crystal, $\Delta\mathbf{R}^c_{t+\Delta t}$, is calculated from incremental spin defined with Eq. (36). With $\Delta\mathbf{R}^c_{t+\Delta t}$ all variables are rotated to the configuration at the end of the increment, $t + \Delta t$.

4. Convergence and accuracy

The purpose of the integration algorithm is to calculate increment in stress. The numerical approximations in integration of rate equations introduce deviation of the calculated stress from the exact value. The difference between the approximated and the exact value of the stress is the global error. The global error is bounded by the truncation error. The truncation error depends on the sub-increment size in numerical integration procedure (Suli and Mayers, 2003). However, since we are dealing with non-smooth functions, originating from conditions controlling the set of active slip systems, the error will be a discontinues function of the sub-increment size. Furthermore, the dominant contribution to the error can be the distance between discontinuity and nearest point at which functions are evaluated. For this reason we will distinguish between the 1st step in which slip systems are being activated during elasto-plastic transition and the 2nd step during which the set of active slip systems does not change. The 2nd step is considerably smaller to ensure no activation of inactive slip systems. The sub-increments are calculated using:

$$\Delta\bar{\boldsymbol{\varepsilon}}^{sub} = \Delta\bar{\boldsymbol{\varepsilon}}\ h \text{ with } h = \frac{1}{n}, \tag{37}$$

where $\Delta\bar{\boldsymbol{\varepsilon}}^{sub}$ is the sub-increment, h is the sub-increment size, and n is the number of sub-steps. With decreasing h the approximated stress increment converges to the exact value at certain rate, referred to as the order of accuracy. A formal order of accuracy quantity is derived from the truncation error (Suli and Mayers, 2003). The explicit and implicit integration methods are expected to have the order of accuracy equal to unity. Here we will evaluate the order of accuracy based on the norm of absolute global error (Veluri et al., 2012):

$$e = \|\bar{\boldsymbol{\sigma}}^h - \bar{\boldsymbol{\sigma}}^{exact}\| = C_h h^p + O(h^{p+1}) \tag{38}$$

where e is the norm of absolute global error, $\bar{\boldsymbol{\sigma}}^h$ is the numerical solution with sub-step size h, $\bar{\boldsymbol{\sigma}}^{exact}$ is the exact solution, p is the order of accuracy, C_h is a scalar constant and $O(h^{p+1})$ are the higher order terms.

Before performing the integration we need to specify the single crystal hardening law by defining the hardening matrix, $h^{ss'}$, used in Eq. (5). A simple hardening law involving three fitting parameters is implemented in both codes:

$$\tau^s_c = \tau_0 + \sum_{s'} L^{ss'}Q(1 - \exp(-b\gamma^{s'})), \tag{39}$$

where $Q = 40$ and $b = 10$ are fitting parameters and $\tau_0 = 16\text{MPa}$ is the initial slip resistance. Only self-hardening is allowed by setting the strength interaction matrix to $L^{ss} = 1$ and $L^{ss'} = 0$. Since an expression for the evolution of slip resistance in function of shear strain on slip system is adopted, elements of the hardening matrix are partial derivatives of slip resistance with respect to the shear strain on the slip system: $h^{ss'} = \frac{\partial\tau^s_c}{\partial\gamma^{s'}} = L^{ss'}bQ\exp(-b\gamma^{s'})$. The modeling framework and integration algorithm are general and can handle any hardening law. The material is Cu. The elastic constants of Cu are $C_{11} = 170\text{GPa}$, $C_{12} = 124\text{GPa}$ and $C_{44} = 75\text{GPa}$ (Anand and Kothari, 1996). The slip family $\{111\}\langle 1\bar{1}0\rangle$, active in face centered cubic (FCC) materials, was considered. 10 orientations shown in Fig. 3a were used as the initial texture. The following two strain increments have been applied:

$$\Delta\bar{\boldsymbol{\varepsilon}}_1 = \begin{bmatrix} 0.03 & 0 & 0 \\ 0 & -0.015 & 0 \\ 0 & 0 & -0.015 \end{bmatrix}, \tag{40a}$$

$$\Delta\bar{\boldsymbol{\varepsilon}}_2 = \begin{bmatrix} 0.004 & 0 & 0 \\ 0 & -0.002 & 0 \\ 0 & 0 & -0.002 \end{bmatrix}. \tag{40b}$$

With very fine sub-increment size the global error should vanish and both explicit and implicit procedure results should converge to the exact value, $\bar{\boldsymbol{\sigma}}^{exact}_1$. For this purpose we use 10,000 sub-steps in explicit and implicit integration and apply $\Delta\bar{\boldsymbol{\varepsilon}}_1$. The norm of difference between evaluated stress by explicit and implicit procedures is 0.03313 MPa. Some possible contributions to this difference are identified next. The solution procedure in the explicit and implicit EPSC is different. In the implicit EPSC the strain increments of single crystals are varied until the residual defined in terms of the single crystal stress increments is below prescribed tolerance. On the other hand, in explicit EPSC the homogenized tangent stiffness is varied using the fixed point iterations, until difference between the new guess and the previous guess for the homogenized tangent stiffness is lower than the prescribed tolerance. Due to differences in the solution procedures, the calculated single crystal variables and the homogenized tangent stiffness are not the same between the explicit and implicit integration schemes, even when

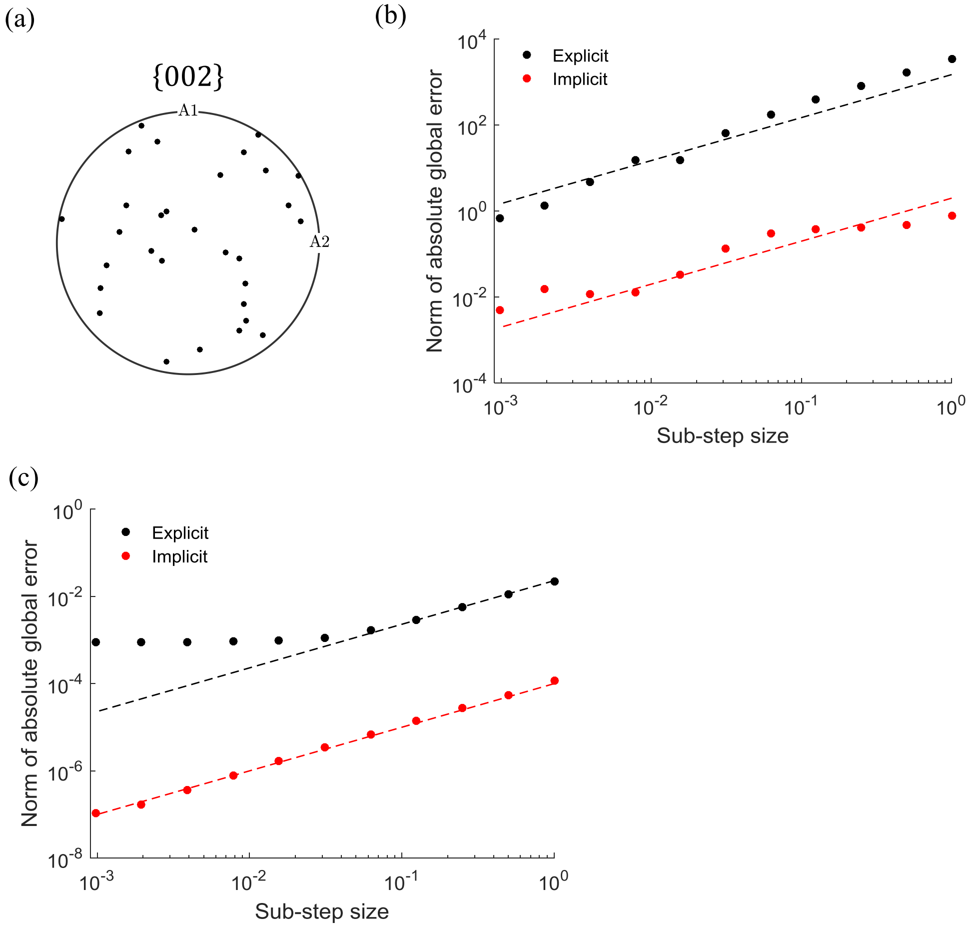

Fig. 3. (a) {002} pole figure showing the initial set of crystal orientations. Calculated norm of the absolute global error, defined with Eq. (51), in function of sub-step size: (a) after applying the first strain increment $\Delta\bar{\boldsymbol{\varepsilon}}_1$ and (b) after applying the second strain increment $\Delta\bar{\boldsymbol{\varepsilon}}_2$ for both explicit and implicit integration procedures.

the tolerances are decreased to very small values for very fine increments. Another source of the difference is the intrinsic sub-incrementation of the single crystal response within the implicit code upon activating an additional slip system, preventing the stress from exiting the single crystal yield surface. In the standard EPSC there is no such scheme, and exit of stress out of the single crystal yield surface is inevitable when slip systems are first activated. The problem can be circumvented by using a large number of sub-steps, which was done here. Since we are interested in convergence of implicit method developed here, we will set $\bar{\boldsymbol{\sigma}}_1^{exact} = \bar{\boldsymbol{\sigma}}_1^{\frac{1}{100,00},imp}$.

We calculate error using Eq. (38) for several sub-step sizes for explicit and implicit integration algorithm under the applied $\Delta\bar{\boldsymbol{\varepsilon}}_1$. The results are plotted in Fig 3b. The points are calculated errors from the explicit and implicit codes for corresponding step sizes, while the lines have slopes of the first order procedure i.e. $p = 1$, and serve as a guide for identifying the order of accuracy. Due to switch conditions for checking the set of active slip systems, the rate of calculated error change with the sub-step size is not constant. The error for the implicit procedure at the same step size is around two orders of magnitude lower than the explicit procedure.

Next, we use identical state after application of $\Delta\bar{\boldsymbol{\varepsilon}}_1$ in both explicit and implicit model and apply $\Delta\bar{\boldsymbol{\varepsilon}}_2$. We evaluate $\bar{\boldsymbol{\sigma}}_2^{exact}$ using 10,000 sub-steps in the implicit procedure. The norm of difference between explicit and implicit solutions with 10,000 sub-steps is 0.0009154 MPa. Fig. 3c shows evaluated norm of error in function of sub-step size for both explicit and implicit codes. Again, the evaluated order of accuracy is unity for both explicit and implicit models. Since we are dealing with very small errors because of the small increment in strain and no activation of inactive slip systems, the tolerances in both explicit and implicit models are tightened to very low values. The error for the explicit model remains constant after reaching 0.001 MPa. This is because the explicit model is not converging to $\bar{\boldsymbol{\sigma}}_2^{exact}$, but to the explicit solution for 10,000 sub-steps which is roughly 0.001 MPa from the adopted $\bar{\boldsymbol{\sigma}}_2^{exact}$.

Results in this section are obtained by running the calculations using double precision i.e. 16 significant digits. In general, besides the truncation error, the roundoff error contributes to the global error (Greenbaum and Chartier, 2012). Next, we evaluate the roundoff error of the implicit algorithm. To this end, we run the simulation with 128 sub-steps using 8, 16 and 32 significant digits representing the floating point numbers. After application of first strain increment, norm of the difference between stresses obtained with 8 and 32 significant digits is 0.24 E − 1, while the same norm calculated with 16 and 32 significant digits is 0.751 E − 2. For all three precisions, the 2nd strain increment is applied from the same initial state as in analysis of the truncation error. The norm of the difference between stresses calculated with 8 and 32 significant digits is 0.353 E − 3, while the same norm with 16 and 32 significant digits is 0.516 E − 11. Note that all cases had the same tolerances, which had to be slightly loosened in order to achieve convergence in cases where 8 significant digits were used in calculations. As is evident, the calculations with different number of significant digits yield similar results further proving the numerical stability of the developed algorithms.

5. Coupling of the implicit EPSC model with implicit finite elements

The coupling is performed with Abaqus through a user material subroutine (UMAT). It is important to note that Abaqus relies on the current configuration to express all tensors and vectors. The current configuration is formed by applying the rigid body rotation to the known configuration at t (Abaqus, 2012). In the description that follows, we will use the subscript FE to denote variables used in the communication with the FE software.

The constitutive relation within finite elements is used to calculate stress at the end of the increment, $\boldsymbol{\sigma}_{FE}^{t+\Delta t}$, based on the guessed total strain increment, $\Delta\boldsymbol{\varepsilon}_{FE}$, which results from the applied boundary conditions over the FE model. The incremental rotation matrix, $\Delta\mathbf{R}_{FE}$, is also provided in UMAT by Abaqus to update the configuration. The algorithm for stress update inside UMAT is as follows:

(1) All tensors in EPSC including crystal orientations are rotated to the configuration at $t + \Delta t$ with $\Delta\mathbf{R}_{FE}$ incremental rotation matrix for consistency with variables from Abaqus, since Abaqus rotates them to $t + \Delta t$ before passing them to UMAT. With respect to the imposed macroscopic rotation the configuration is $t + \Delta t$. However, the single crystal rotation due to the applied strain increment from Abaqus is unknown beforehand. Therefore, all crystal quantities will be kept at t with respect to the single crystal rotation.

(2) Total strain at a material point at the end of the time increment is:

$$\boldsymbol{\varepsilon}_{FE}^{t+\Delta t} = \boldsymbol{\varepsilon}_{FE}^{t} + \Delta\boldsymbol{\varepsilon}_{FE}. \tag{41}$$

where $\boldsymbol{\varepsilon}_{FE}^{t+\Delta t}$, $\boldsymbol{\varepsilon}_{FE}^{t}$ and $\Delta\boldsymbol{\varepsilon}_{FE}$ are the total strain at the end of the time increment, the strain at the beginning of the increment, and the strain increment, respectively. The total strain at the end of the time increment corresponds to the total strain accommodated by the HEM material point at the end of the time increment, while the total stress returned to the Abaqus corresponds to the stress in the HEM. Therefore, the following conditions are valid:

$$\boldsymbol{\varepsilon}_{FE}^{t+\Delta t} = \boldsymbol{\varepsilon}_{FE}^{t} + \Delta\boldsymbol{\varepsilon}_{FE} = \langle \boldsymbol{\varepsilon}^{c,t+\Delta t} \rangle = \langle \Delta\mathbf{R}_{t+\Delta t}^{c} (\bar{\boldsymbol{\varepsilon}}^{c,t} + \Delta\bar{\boldsymbol{\varepsilon}}^{c}) \Delta\mathbf{R}_{t+\Delta t}^{c}{}^{T} \rangle \tag{42a}$$

$$\boldsymbol{\sigma}_{FE}^{t+\Delta t} = \langle \boldsymbol{\sigma}^{c,t+\Delta t} \rangle = \langle \Delta\mathbf{R}_{t+\Delta t}^{c} (\bar{\boldsymbol{\sigma}}^{c,t} + \Delta\bar{\boldsymbol{\sigma}}^{c}) \Delta\mathbf{R}_{t+\Delta t}^{c}{}^{T} \rangle \tag{42b}$$

In Eq. (42a) the strain at the beginning of the time increment, $\bar{\boldsymbol{\varepsilon}}^{c,t}$, and the total strain from the FE software, $\boldsymbol{\varepsilon}_{FE}^{t+\Delta t}$, are known. The crystal strain increment, $\Delta\bar{\boldsymbol{\varepsilon}}^{c}$, stress increment, $\Delta\bar{\boldsymbol{\sigma}}^{c}$, and incremental rotation matrix, $\Delta\mathbf{R}_{t+\Delta t}^{c}$, are calculated by performing the numerical integration described in Section 3 under the imposed strain increment, $\Delta\bar{\boldsymbol{\varepsilon}}$. Note that the single crystal strain increment, $\Delta\bar{\boldsymbol{\varepsilon}}^{c}$, can be expressed in terms of the applied polycrystalline strain increment, $\Delta\bar{\boldsymbol{\varepsilon}}$, using the localization tensor, $\bar{\mathbf{A}}^{c}$, defined with Eq. (15), as: $\Delta\bar{\boldsymbol{\varepsilon}}^{c} = \bar{\mathbf{A}}^{c}\Delta\bar{\boldsymbol{\varepsilon}}$. Also, the incremental rotation matrix, $\Delta\mathbf{R}_{t+\Delta t}^{c}$, is calculated from the total incremental spin, $\bar{\mathbf{W}}^{c}\Delta t$, defined with Eq. (36), where $\bar{\mathbf{W}}^{c}\Delta t$ is dependent on the imposed strain increment $\Delta\bar{\boldsymbol{\varepsilon}}$. In presence of crystal rotations, the imposed strain increment, $\Delta\bar{\boldsymbol{\varepsilon}}$, satisfying the Eq. (42a), is not equal to $\Delta\boldsymbol{\varepsilon}_{FE}$. This is clearly seen by looking at the first strain increment $\Delta\boldsymbol{\varepsilon}_{FE}$. Imposing the increment $\Delta\boldsymbol{\varepsilon}_{FE}$ in the integration procedure enforces Eq. (13) in the incremental form: $\Delta\boldsymbol{\varepsilon}_{FE} = \langle \Delta\bar{\boldsymbol{\varepsilon}}^{c} \rangle$. Once the update due to crystal rotation is performed the equality no longer holds: $\Delta\boldsymbol{\varepsilon}_{FE} \neq \langle \Delta\mathbf{R}_{t+\Delta t}^{c}\Delta\bar{\boldsymbol{\varepsilon}}^{c}\Delta\mathbf{R}_{t+\Delta t}^{c}{}^{T} \rangle$. However, if an appropriate strain increment $\Delta\bar{\boldsymbol{\varepsilon}}$ is applied instead of $\Delta\boldsymbol{\varepsilon}_{FE}$ the condition $\Delta\boldsymbol{\varepsilon}_{FE} = \langle \Delta\mathbf{R}_{t+\Delta t}^{c}\bar{\mathbf{A}}^{c}\Delta\bar{\boldsymbol{\varepsilon}}\Delta\mathbf{R}_{t+\Delta t}^{c}{}^{T} \rangle$ can be satisfied. Similar analysis can be performed for any subsequent increment. Therefore, Eq. (42a) represents a set of 6 non-linear equations in terms of the unknown imposed strain increment, $\Delta\bar{\boldsymbol{\varepsilon}}$. Solving Eq. (42a) for $\Delta\bar{\boldsymbol{\varepsilon}}$ involves an iterative procedure, in which for each iteration a new guess for $\Delta\bar{\boldsymbol{\varepsilon}}$ is made. For each guess for $\Delta\bar{\boldsymbol{\varepsilon}}$, the integration procedure (Section 3) is performed. Since the integration procedure is where majority of time is spent in UMAT, the simulation time is increased significantly with each new guess for $\Delta\bar{\boldsymbol{\varepsilon}}$. To avoid the expensive iterations, the Eq. (42a) is rewritten, neglecting the effect of crystal rotations within current increment i.e. $\Delta\mathbf{R}_{t+\Delta t}^{c}$ is set to identity:

$$\boldsymbol{\varepsilon}_{FE}^{t} + \Delta\boldsymbol{\varepsilon}_{FE} = \langle \bar{\boldsymbol{\varepsilon}}^{c,t} \rangle + \langle \Delta\bar{\boldsymbol{\varepsilon}}^{c} \rangle. \tag{43}$$

Using Eq. (13), enforced by the homogenization procedure in the incremental form, allows for a straight forward calculation of the imposed strain increment from Eq. (43):

$$\Delta\bar{\boldsymbol{\varepsilon}} = \boldsymbol{\varepsilon}_{FE}^{t} + \Delta\boldsymbol{\varepsilon}_{FE} - \langle \bar{\boldsymbol{\varepsilon}}^{c,t} \rangle. \tag{44}$$

(3) Numerical integration described in Section 3 is performed with imposed strain increment defined with Eq. (44). The integration can be performed with the calculated increment in strain from Eq. (44), or any sub-increments of $\Delta\bar{\boldsymbol{\varepsilon}}$, if the macroscopic sub-incrementation is chosen.

(4) Using the same approach for Eq. (42b) as for Eq. (42a) allows the calculation of stress at the end of the time increment:

$$\boldsymbol{\sigma}_{FE}^{t+\Delta t} = \langle \bar{\boldsymbol{\sigma}}^{c,t} \rangle + \langle \Delta\bar{\boldsymbol{\sigma}}^{c,t} \rangle = \langle \bar{\boldsymbol{\sigma}}^{c,t} \rangle + \Delta\bar{\boldsymbol{\sigma}} \tag{45}$$

(5) All tensors referring to crystal frames are rotated for the crystal incremental rotation matrix, $\Delta\mathbf{R}_{t+\Delta t}^{c}$, calculated from spin acting over increment in time Δt using Eq. (36). In other words, the configuration with respect to single crystal rotation is updated to $t + \Delta t$ at the very end of the procedure.

In addition to the stress update procedure, the Jacobian, $\frac{\partial\Delta\boldsymbol{\sigma}_{FE}}{\partial\Delta\boldsymbol{\varepsilon}_{FE}}$, needs to be calculated in order to obtain a new guess for the incremental displacement field in the non-linear implicit FE analysis. The derivative is:

$$\frac{\partial\Delta\boldsymbol{\sigma}_{FE}}{\partial\Delta\boldsymbol{\varepsilon}_{FE}} = \frac{\partial(\boldsymbol{\sigma}_{FE}^{t+\Delta t} - \boldsymbol{\sigma}_{FE}^{t})}{\partial\Delta\boldsymbol{\varepsilon}_{FE}} = \frac{\partial\Delta\bar{\boldsymbol{\sigma}}}{\partial\Delta\bar{\boldsymbol{\varepsilon}}} = \frac{\partial(\bar{\mathbf{L}}^{inc}\Delta\bar{\boldsymbol{\varepsilon}})}{\partial\Delta\bar{\boldsymbol{\varepsilon}}} = \bar{\mathbf{L}}^{inc} \tag{46}$$

The bars denote that all quantities, including the Jacobian, are evaluated consistently with Eqs. (44) and (45) in the configuration at t with respect to the single crystal rotation. It should be noted that the analytical evaluation of the Jacobian presented here is much more elegant than that presented in the original FE-EPSC implementation (Zecevic et al., 2017) because the rotation and deformation effects are decomposed and single crystal rotation during the current time increment is filtered when the stress at the end of the time increment is updated with Eq. (45). In Zecevic et al. (2017) several sub-steps were used and the configuration was updated after each sub-step, resulting in complicated dependence of the increment in stress on the applied strain increment. It should be noted that the developed stress update procedure and the Jacobian calculation are independent on the integration algorithm and can be used both with the original explicit and with the newly developed implicit integration. The difference between the implicit integration vs. the explicit integration is only present in step 3 of the stress update procedure.

As will be shown later, the sub-steps are not necessary in the implicit implementation because it can handle large increments. The increments driven by Abaqus can be used, while the original explicit EPSC implementation in implicit finite elements relied on a sub-stepping algorithm. It was possible to use increments driven by Abaqus in the original implementation but the calculations were inaccurate, which is the intrinsic limitation of any explicit solution procedure. Therefore, in the current study, we have simplified the Jacobian, ensured the accurate solution with large increments with no need for sub-stepping of those passed by Abaqus, and as a result gained the computational efficiency.

6. Simulations using FE-EPSC

In this section, the multi-level FE-EPSC model incorporating the implicit EPSC is benchmarked using the single crystal data for Cu and

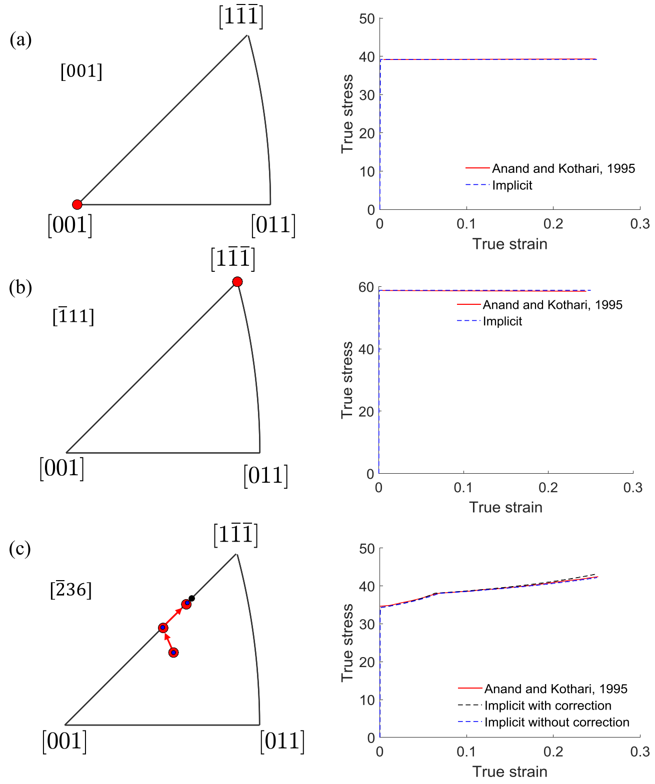

Fig. 4. Comparison of the predicted crystal lattice reorientation and true stress-true strain response under simple tension for three single crystals. The loading axis relative to the crystal frame is indicated for each single crystal.

then applied to simulate drawing of a cup from an aluminum alloy AA6022-T4 sheet.

6.1. Benchmark case study: single crystals

Single crystal tension simulations without hardening performed in Anand and Kothari (1996) are used to validate the single crystal integration algorithm and texture update algorithm. One brick continuum finite element with 8 nodes and 8 integration points in three-dimensional space (labeled as C3D8 in Abaqus convention) is used. The model is set consistent with the simulation setup presented in Anand and Kothari (1996). The slip systems belonging to $\{111\}\langle 1\bar{1}0\rangle$ family are allowed to activate. The entries of the hardening matrix are set to sufficiently small values, $h^{ss'} = 0.01$. The results of simulations for three different crystal orientations are shown in Fig. 4. As expected, the orientations [001] and [$\bar{1}$11] are stable, while [$\bar{2}$36] is not stable but evolves. The results show good match between the approach presented here and the one used in Anand and Kothari (1996). Some differences in the rate of crystal reorientation and stress level are seen for the tension of [$\bar{2}$36] orientation. We attribute the mismatch to the difference in the formulation used here and that used in Anand and Kothari (1996). The major source of mismatch is the assumed update of plastic deformation gradient given with relation (41) in Anand and Kothari (1996):

$$\mathbf{F}^p_{t+\Delta t} = \left(\mathbf{I} + \sum_s \Delta\gamma^s \; sign(\tau_t^s)\mathbf{b}_t^s \otimes \; \mathbf{n}_t^s\right)\mathbf{F}^p_t, \tag{47}$$

where $\mathbf{F}^p$ is plastic deformation gradient. Enforcing small time increments, we can assume $\Delta\gamma^s \ll 1$ and $\Delta\gamma^s \; \Delta\gamma^{s'} \;\approx 0$. Expanding the relation for n number of steps and disregarding higher order terms in $\Delta\gamma^s$:

$$\mathbf{F}^p_n = \mathbf{I} + \sum\nolimits_i \sum\nolimits_s \Delta\gamma_i^s \; sign(\tau_i^s)\mathbf{b}_i^s \otimes \; \mathbf{n}_i^s. \tag{48}$$

The actual plastic deformation gradient after n steps is:

$$\mathbf{F}^p_n = \mathbf{I} + \sum\nolimits_i \sum\nolimits_s \Delta\gamma_i^s \; sign(\tau_i^s)\mathbf{b}_n^s \otimes \; \mathbf{n}_n^s. \tag{49}$$

Incremental update of plastic deformation gradient does not account for the contribution coming from the rotation of crystal with accumulated shear strain on slip systems. To verify that this effect is indeed the source of the difference we compare the results of tension of [$\bar{2}$36] orientation from Anand and Kothari (1996) with two modeling approaches within implicit EPSC model. The first approach relies on the strain increment correction procedure in Section 4. The method corrects the applied strain increment from Abaqus with a “strain increment” originating from an additional single crystal rotation of the total strain in the crystal. The additional rotation is present due to the plastic spin. The model predicts slightly higher stress and more rapid reorientation of single crystal orientation as can be seen in Fig. 4c. The second modeling approach neglects the effect of plastic spin on rotation of total strain tensor and simply applies the total strain increment from Abaqus. The comparison with the first modeling method and the result from Anand and Kothari (1996) is shown in Fig. 4c. Both the stress strain response and the crystal reorientation are closer to those presented in Anand and Kothari (1996).

6.2. Application case study: deep drawing of AA6022-T4

In this section the implicit integration procedure is used in conjunction with an advanced dislocation density-based hardening law considering the kinematic backstress effects. The hardening model has been calibrated in Zecevic and Knezevic (2018) to predict anisotropic mechanical response during monotonic loading as well as linear and non-linear unloading, the Bauschinger effect and hardening rates upon the load reversal for AA6022-T4. Most generically, the model accounts for the development of intra-granular backstresses, backstress aided dislocation glide, thermally activated storage of dislocations, elastic anisotropy, inter-granular stresses, and crystallographic slip. The law is summarized in the Appendix A.

The hardening law is further adjusted here to achieve match with several cyclic stress strain curves (Fig. 6). Tables 1 and 2 show the established material parameters. Using these new parameters, the comparison between measured and calculated results for the monotonic tension in RD, 45°, and TD, and corresponding r-values is shown in Fig. 5. The anisotropy in the simulated flow curves, seen in Fig. 5a, is attributed to an accurate latent hardening description with the experimentally evaluated strength interaction matrix, L, (Kocks and Brown, 1966). It should be noted that the r-values, shown in Fig. 5b, are predictions. These predictions are found to be not very sensitive to the hardening law fitting parameters. The backstress fitting parameters and the reversible dislocations parameters, described in Appendix A, are fit by comparing the simulated and the measured cyclic response in RD, shown in Fig. 6. The model slightly over-predicts the amount of

Table 1
Constitutive parameters for the evolution of slip resistance for $\{111\}\langle 1\bar{1}0\rangle$ slip mode in AA6022-T4. Note that coplanar slip systems have the interaction term of 1, while non-coplanar slip systems have the interaction term of 1.4 in latent hardening matrix.

$L^{ss'}_{coplanar}$	$L^{ss'}_{non-coplanar}$	g^{ss}	$g^{ss'}$	τ_0[MPa]	$k_1[m^{-1}]$	g	D[MPa]	q	p
1.0	1.4	1	1	58	0.65×10^8	0.0294	100	4	0.3

Table 2
Parameters for the evolution of slip system kinematic backstress in AA6022-T4.

τ_{bs}^{sat} [MPa]	ν	γ_b	A
5	560	0.001	1

permanent softening i.e. the drop in the stress level during the compression in comparison to the initial tension. A possible cause of the discrepancy between the simulated and measured cyclic curves is the over-predicted inter-granular residual stress. The EPSC formulation is closer to the Taylor iso-strain than to the Sachs isostress homogenization assumption (Zecevic and Knezevic, 2018). The inter-granular residual stresses are large in the Taylor homogenization, while the Sachs homogenization does not predict the appearance of inter-granular residual stresses. The inter-granular residual stresses are known to influence the cyclic behavior of materials (Li et al., 2014; Wu et al., 2005; Zecevic and Knezevic, 2015). The comparisons in Fig. 6 confirm that the non-linearity of unloading increases with the amount of pre-strain and that the backstresses have a dominant effect in capturing non-linear unloading while both the backstresses and inter-granular stresses govern the BE. Moreover, the inclusion of reversible dislocation motion is the key for capturing hardening rates during reverse loading. It is worth pointing out that the same calculation results can be obtained using the standard explicit EPSC model.

The simulation results in Figs. 5 and 6 are shown for 219 orientations representing the ODF reconstructed from an EBSD scan. Since the run time of any EPSC simulation is proportional to the number of crystals used, the ODF is represented with a minimum number of orientations that still give representative mechanical response of the material based on the procedure described in Eghtesad et al. (2018b) and Knezevic and Landry (2015).

Fig. 7 shows the deep drawing simulation set up and the blank mesh (Zecevic and Knezevic, 2017). The set up consists of a die, a blank holder, and a punch. The friction coefficient is set to 0.1. The punch, the die, and the blank holder are modeled as analytical rigid surfaces. The blank thickness is 1.2 mm, which is modeled with 5 integration points through the thickness. During the simulation blank holder is held fixed at 1.2 mm from the die, while the punch is displaced downwards in order to draw the cup. After drawing, the contact between the drawn cup, punch, die and blank holder is removed in order to simulate springback. Only one quarter of the cup was modeled due to the orthotropic texture (Fig. 5a). The blank mesh size was determined based on a mesh-sensitivity study. Three mesh sizes were tested: coarse (25 S3R and 975 S4R shell elements), medium (50 S3R and 3900 S4R shell elements) and fine (100 S3R and 15,600 S4R shell elements). The medium mesh is shown in Fig 7b. J_2 material behavior i.e. the von Mises yield surface, was used for mesh sensitivity study. The yield stress in function of the equivalent plastic strain was entered in a tabular form to reproduce the simple tension true stress-true strain curve in the RD. The medium mesh is used for testing the implicit EPSC UMAT implementation since it provides sufficient accuracy for this purpose.

6.2.1. *Effect of increment size on speed and accuracy*

In order to determine an appropriate UMAT increment size the drawing simulation was first run with a J_2 material behavior i.e. the von Mises yield surface. The objective was to maximize the time increment, while preserving the accuracy of the simulation. The total equivalent strain at the material point was 0.48, split into 130 strain increments. The strain history in the form of three strain components has been extracted during the drawing step from the highlighted element in Fig 7b. Fig. 8a shows the recorded strain history. The strain history is imposed along with zero stress 13, 23, and 33 components to generate the stress history by both explicit and implicit integration procedures. Similar to Eq. (38), we define a norm of a relative global error in terms of total stress at each increment:

$$e^{inc} = \left. \frac{\|\bar{\sigma}^{h} - \bar{\sigma}^{exact}\|}{\|\bar{\sigma}^{exact}\|} \right|_{inc}, \tag{50}$$

where $\bar{\sigma}^{h}$ is the numerically evaluated stress with a sub-increment size h at the end of the increment *inc* and $\bar{\sigma}^{exact}$ is the exact value of stress at the end of the increment *inc*. In Section 5 we used the implicit solution

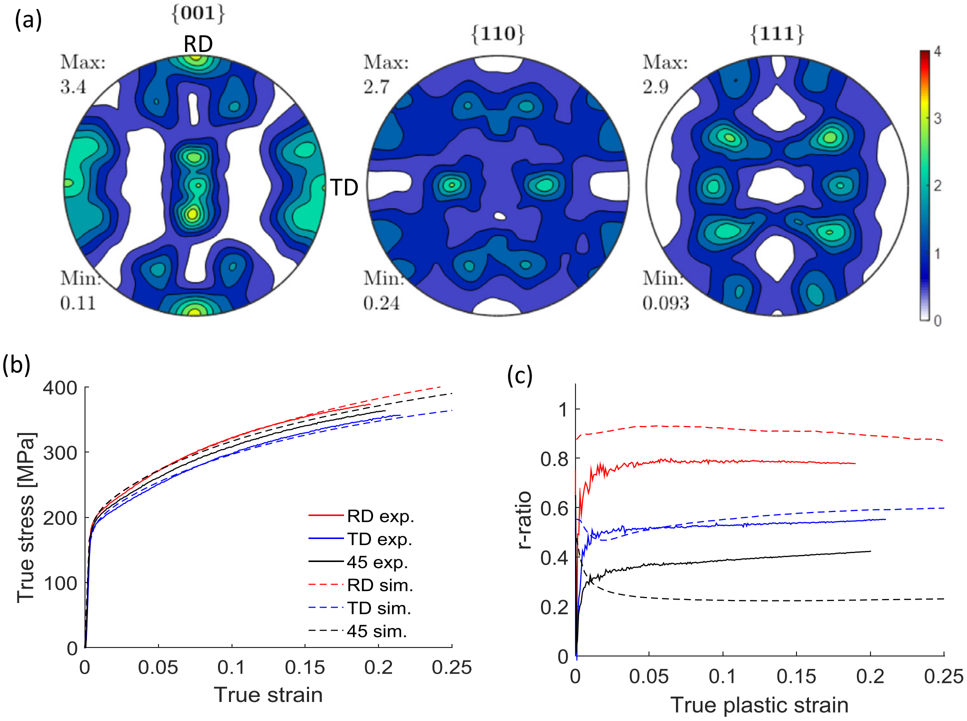

Fig. 5. (a) Measured texture of AA6022-T4 sheet. Comparison between measured and simulated mechanical response of AA6022-T4: (b) monotonic true stress-true strain curves along the three loading directions as indicated in the legend, (c) evolution of r-ratio along the same three loading directions as in (b).

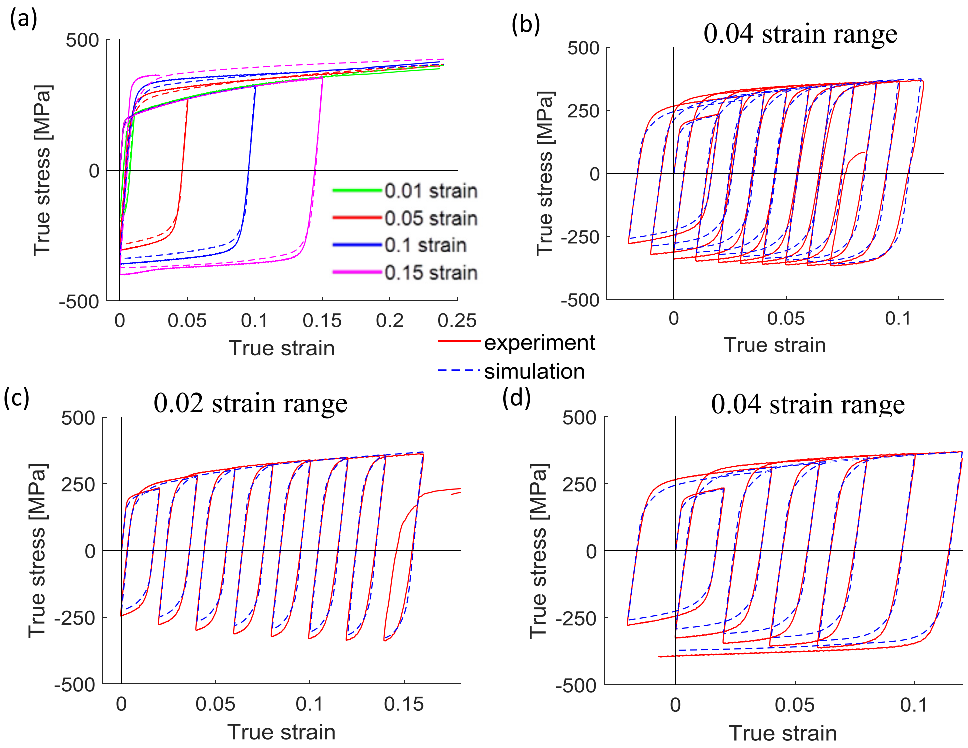

Fig. 6. Comparison of measured and calculated true stress-true strain response for alloy AA6022-T4 along RD during: (a) one strain cycle to four pre-strain levels as indicated in the legend followed by tension until failure, (b) multiple strain cycles with a constant strain range of 0.04 and increasing mean strain in increments of 0.01 from 0 for the 1st cycle to 0.09 for the 10th cycle, (c) multiple strain cycles with a constant strain range of 0.02 and increasing mean strain in increments of 0.02 from 0.01 for the 1st cycle to 0.15 for the 8th cycle, and (d) multiple strain cycles with a constant strain range of 0.04 and increasing mean strain in increments of 0.02 from 0.0 for the 1st cycle to 0.1 for the 6th cycle ending with compression until failure.

with 10,000 sub-steps as $\bar{\boldsymbol{\sigma}}^{exact}$, since we were interested in convergence of the implicit procedure and we were dealing with very small errors. Here we use a similar approach and set $\bar{\boldsymbol{\sigma}}^{exact}$ to be the implicit solution with 100 sub-steps for each increment coming from Abaqus with no sub-stepping for the integration at the single crystal level. The calculated stress history is shown in Fig 8b. To validate the calculated $\bar{\boldsymbol{\sigma}}^{exact}$, we evaluate the stress history with explicit model with 500 sub-steps, see Fig 8b. The relative error defined with Eq. (50) for explicit model with 500 sub-steps is shown in Fig 8c. Interestingly, the difference is smaller if latent hardening and backstress are not considered (Fig. 8d). Here, the difference between stress histories calculated by the explicit and implicit algorithms is below 0.2%, as seen from Fig 8d. The corresponding norm of imposed strain increment components is approximately 10^{-5} for the explicit and 5×10^{-5} for the implicit procedure. As noted, the consideration of latent hardening and backstress in the model amplify the difference between the explicit and implicit EPSC. The difference starts to develop upon the strain path change. The introduction of the latent hardening values larger than the self-hardening into EPSC is coupled with numerical singularities (Anand and Kothari, 1996; Hill, 1966; Mánik and Holmedal, 2014; Peirce et al., 1982). To overcome the numerical issues several procedures were developed in Zecevic and Knezevic (2018). Close to singular matrices have large condition numbers and amplify differences in vector of knowns between the explicit and implicit EPSC models. The fitted backstress parameters from Table 2 produce a rapid increase of backstress, making the equations governing the evolution of backstress in rate form stiff. Even with very large number of steps overshoot can occur for some crystals. Disabling the backstress and latent hardening and comparing stress histories from the explicit and implicit EPSC models shows significantly lower mismatch (Fig 8d). The parameters for the dislocation based hardening law without latent hardening have been established in Zecevic and Knezevic (2018) and are reported in Table 3.

To study tradeoffs between computational time and accuracy in terms of the sub-step size, the number of sub-steps was varied and the results were compared against the same “accurate” stress history as used for Fig. 8. In the explicit integration procedure the number of increments was decreased from 500 to 250, 100, 50 and 10 and the obtained stress histories were compared against the stress history produced with 500 increments. For the implicit integration procedure, the number of sub-steps was decreased to 10 and then to 2 and finally to 1 per imposed increment in strain from Abaqus, while no sub-stepping was used for the integration at the single crystal level. Additionally, a case with 2 sub-steps in the integration of the single crystal response and no sub-stepping per strain increment from Abaqus was tested. The

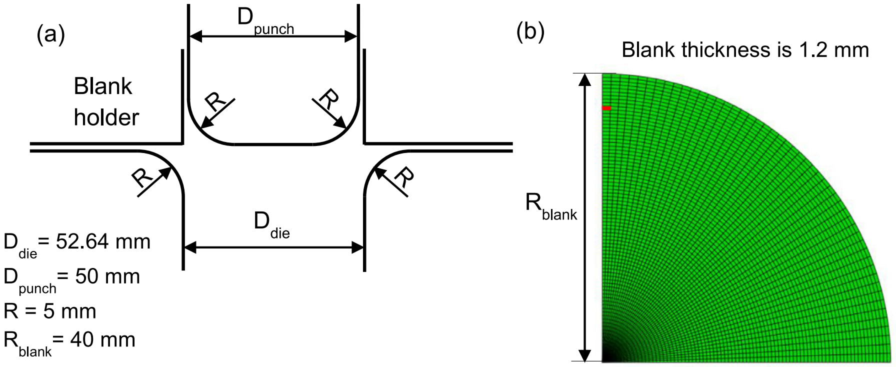

Fig. 7. Simulation setup: (a) deep drawing geometry and (b) FE quarter model of the initial blank containing 3950 shell elements. 79 elements are along the diameter and 50 elements are along the circumference of the blank. One element is highlighted in red to indicate the location of extracted strain history used in the next section.

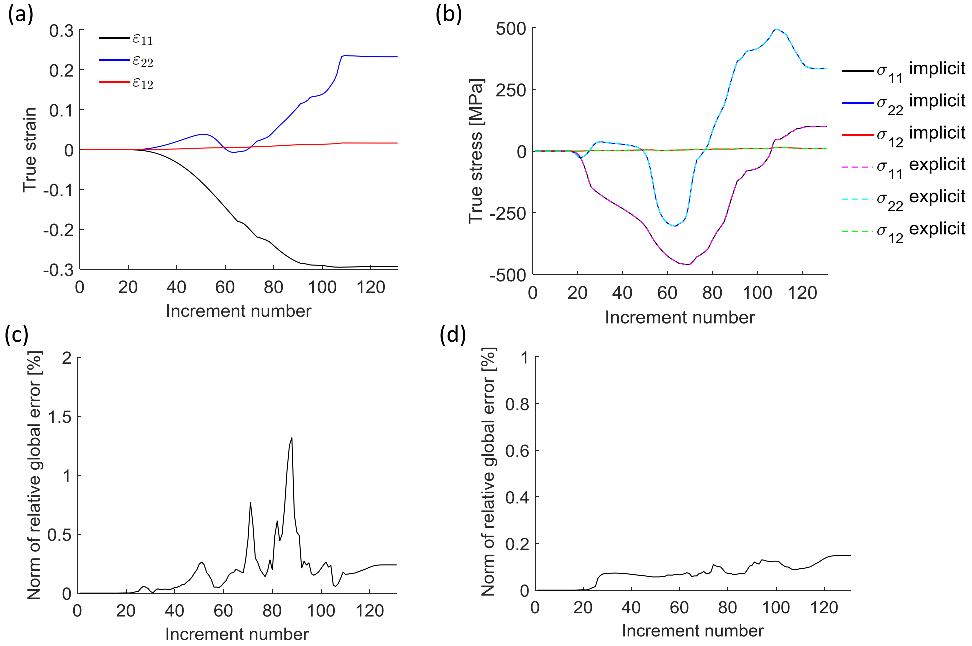

Fig. 8. (a) Imposed strain history. (b) The stress histories generated by the explicit and implicit integration algorithms with sufficient number of sub-steps and (c) the difference between them. (d) The difference like in (c) without considering the latent hardening and backstress effects.

Table 3
Constitutive parameters for the evolution of slip resistance for $\{111\}\langle 1\bar{1}0\rangle$ slip mode in AA6022-T4 without the consideration of latent hardening and slip system interaction in terms of evolution of dislocation densities. Note that there is only self hardening, meaning that the diagonal of the latent hardening matrix is set to 1, while all other terms are set to 0.

L^{ss}	$L^{ss'}$	g^{ss}	$g^{ss'}$	τ_0[MPa]	$k_1\,[m^{-1}]$	g	D[MPa]	q
1	0	1	0	60	3.0×10^8	0.1176	100	8

generated stress histories from these varying number of sub-steps were compared with the "accurate" stress history generated with 100 sub-steps in every imposed strain increment.

In Section 5 we have shown that for the same global error the explicit procedure has a smaller sub-increment size than the implicit procedure, see Fig 3b and c. The reduced number of steps for the same accuracy in the implicit integration, compared to the explicit integration procedure, should be reflected in the computational time of simulations. The computational time comparison is shown in Fig 9a for several practical choices for sub-increment size. The plotted results are calculated as averages of three runs. The average error is calculated from the norm of relative global error as:

$$\text{Average error }[\%] = \frac{1}{ninc}\sum_{inc=1}^{ninc} e^{inc} \tag{51}$$

where $ninc = 130$ is the total number of increments. Increasing the number of sub-steps in the integration procedure results in the increase of the computational time and the decrease of the average error for both codes, as expected. The comparison of computational times between the explicit and implicit code shows that for the same level of accuracy, the implicit code is faster. The ratio of the computational times between the explicit and implicit codes is plotted In Fig 9b. As is evident, the implicit code is at least 3.5 times faster than the explicit code for the same accuracy for the ideal case of no sub-stepping in the implicit formulation.

As mentioned above, the objective in FE-EPSC simulations is to utilize increments driven by Abaqus meaning without introduction of any sub-stepping, although it is an option to specify in the model. The objective is also to use minimum number of sub-steps for the

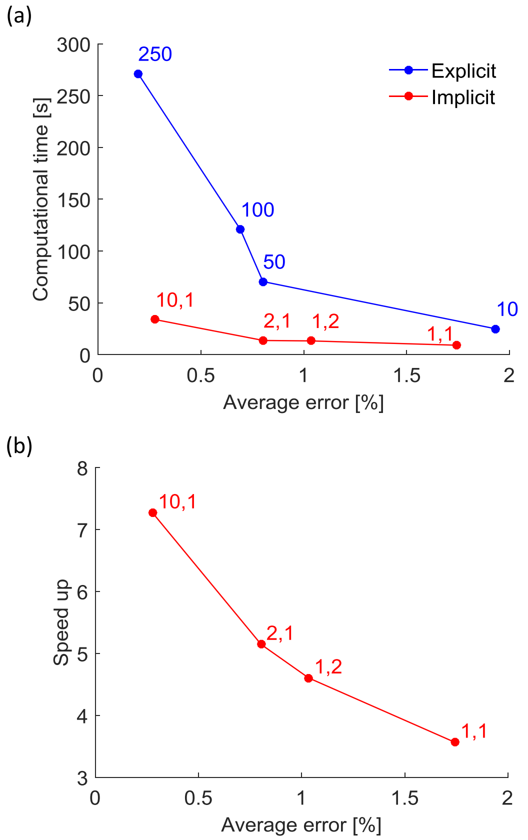

Fig. 9. (a) Computational time involved in the explicit and implicit integration procedures as a function of number of sub-steps. The number next to the explicit model points refers to the number of sub-steps in dividing the Abaqus strain increment, while the numbers next to the implicit model points refer to the number of sub-steps in dividing the Abaqus strain increment and the number of sub-steps used in the single crystal integration procedure, respectively. (b) Speed up of the implicit code relative to the explicit code for the same average error, calculated as the ratio of the explicit to the implicit computational times shown in (a).

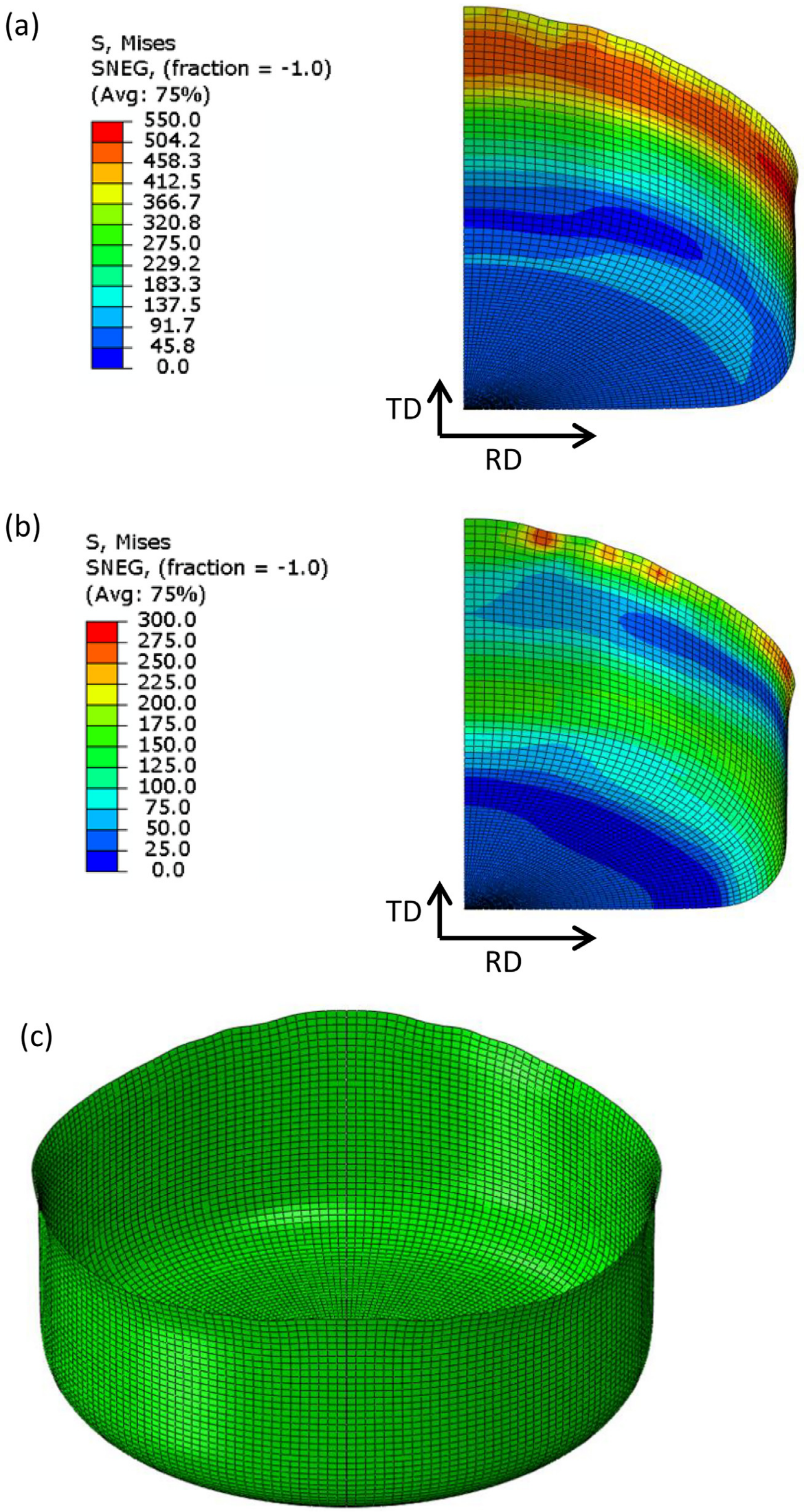

Fig. 10. Deformed mesh with contours of von Mises stress (a) after forming and (b) after springback. (c) Deformed mesh after springback.

integration at the single crystal level, while retaining desired accuracy and reducing computational time required by explicit integration algorithm. In addition to user specified number of sub-steps in integration at single crystal level, intrinsic sub-incrementation due to activation of an additional slip system can occur. The results presented above show that the objectives of the developed implicit integration algorithm are well accomplished. For the cup drawing simulation we applied 2 sub-steps for the division of total strain increment from Abaqus and used no sub-stepping for the single crystal integration procedure because this combination provides the best tradeoff between speed and accuracy.

6.2.2. *Simulation results*

The deformed mesh with contours of von Mises stress for the implicit EPSC UMAT is shown in Fig 10. Texture evolution introduces

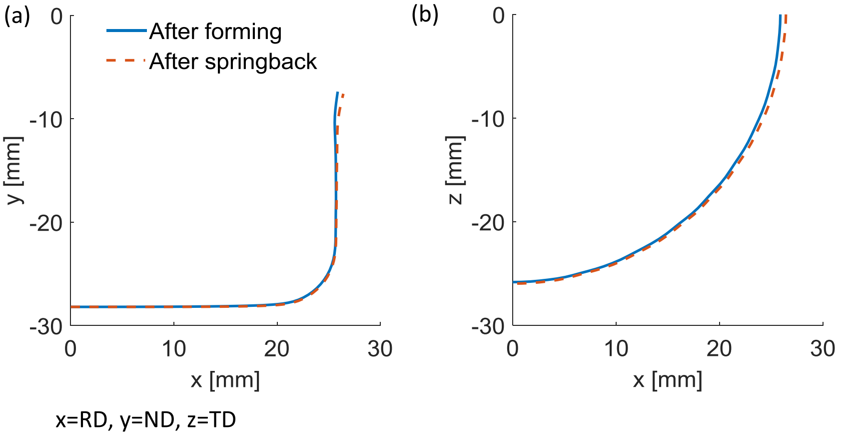

Fig. 11. Prediction of shape: (a) the y-z profile of the drawn cup and (b) the circumference of the drown cup edge in x-z plane.

anisotropy in the mechanical response, which governs the shape evolution of the drawn cup (Fig 10a). After forming, the springback is simulated by fixing the node in the center of the formed cup and maintaining applied symmetries in the RD-ND and TD-ND planes. To suppress the occurrence of geometrical instabilities during springback step, artificial damping available in Abaqus is utilized (Zecevic and Knezevic, 2017; Abaqus, 2012). The resulting contours of von Mises residual stress are shown in Fig 10b. The shape of the cup after springback is compared with the shape of the cup after forming in terms of the nodal positions along RD direction and along the circumference of the cup edge in RD-TD plane in Fig 11a and b, respectively. In closing, it is worth mentioning that the overall computational time involved in the simulation using FE-EPSC was 25.5 h. The job was run on a workstation with dual socket Intel® Xeon® CPU E5-2695 v4 @ 2.1GHz using 35 CPUs. The model is regarded as accurate but also as computationally intensive.

7. Conclusions

This work has developed an implicit integration algorithm for the EPSC polycrystal plasticity model. The rate forms of single crystal and polycrystal constitutive equations are replaced with corresponding incremental forms. An implicit integration algorithm at a single crystal level is used to derive the incremental form of the single crystal constitutive equation. In doing so, a system of non-linear equations is defined and conveniently solved using the fixed point method. With the developed solution procedure for single crystals, a suitable set of non-linear equations is derived from the self-consistent homogenization in incremental form and solved for single crystal strain increments using the Newton's method. The implicit EPSC model is validated first using the original explicit EPSC model. Next, the implicit EPSC is implemented into a stress update algorithm within UMAT subroutine to facilitate the coupling with Abaqus. The implicit EPSC is capable of applying the total strain increment from Abaqus. Here, every material point in the FE mesh is a polycrystal that deforms by anisotropic elasticity and crystallographic slip allowing for the heterogeneous deformation prediction that can occur across a sample as a result of workpiece geometry and material elastic and plastic anisotropy. The coupling is validated against the data from Anand and Kothari (1996) for tension of single crystal Cu. Finally, a finite element simulation of cup drawing of AA6022-T4 with shell elements is performed to illustrate the potential and efficiency of the developed implicit multi-level framework. The evolution of texture, anisotropic hardening, BE, and non-linear unloading were all taken into account in this simulation. The dimensional changes of the cup along with the non-uniform residual stress-strain distribution after drawing in the clamped condition as well as in the free state were predicted.

Acknowledgments

This work is based upon a project supported by the U.S. National Science Foundation under a CAREER grant no. CMMI-1650641. The authors gratefully acknowledge this support. MZ also acknowledges financial support from the University of New Hampshire (UNH)'s Dissertation Year Fellowship (DYF) program.

Supplementary materials

Supplementary material associated with this article can be found, in the online version, at doi:10.1016/j.mechmat.2019.103065.

Appendix A

In the notation used here, indices $s+$ and s- refer to arbitrarily chosen positive and negative directions of slip systems, respectively. Both positive and negative directions are included in index s. The hardening law for the evolution of slip resistance is based on dislocation densities and is temperature and strain rate sensitive (Beyerlein and Tomé, 2008; Jahedi et al., 2015; Knezevic et al., 2014a, 2012, 2014b; Knezevic et al., 2015). Here we summarize the formulation of dislocation based hardening law developed for prediction of anisotropy in mechanical response of aluminum alloy AA6022-T4 (Zecevic and Knezevic, 2018). Reader is referred to (Zecevic and Knezevic, 2018) for detailed description of the hardening law.

The slip resistance is defined as:

$$\tau_c^s = \tau_0^\alpha + \tau_{forest}^s + \tau_{debris}^\alpha, \tag{A1}$$

where τ_0^α is an initial slip resistance, τ_{forest}^s is a contribution to slip resistance from statistically stored dislocations, τ_{debris}^α is a is a contribution to slip resistance from dislocations stored as debris. The forest contribution to slip resistance is:

$$\tau_{forest}^s = b^\alpha \chi \mu^\alpha \sqrt{\sum_{s'} L^{ss'} \rho_{tot}^{s'}} \tag{A2}$$

where $b^{\alpha} = 2.86\ 10^{-10}$ m is the Burgers vector for aluminum, $\chi = 0.9$ is an interaction constant, ρ_{tot}^{s} is the total forest dislocation density for s^{th} slip system belonging to α slip mode ($s \in \alpha$) and $L^{ss'}$ is a strength interaction matrix (Franciosi and Zaoui, 1982; Khadyko et al., 2016). From single crystal experiments (Kocks and Brown, 1966) the entries of strength interaction matrix have been evaluated to be 1 for coplanar slip systems and 1.4 for all other interactions. However, such strength interaction coefficients lead to the loss of ellipticity of the single crystal and macroscopic tangent modulus. A diagonalization procedure of hardening matrix is developed in Zecevic and Knezevic (2018) to treat the problem.

The debris contribution to slip resistance is:

$$\tau_{debris}^{\alpha} = k_{deb}\mu^{\alpha} b^{\alpha}\sqrt{\rho_{deb}}\,log\left(\frac{1}{b^{\alpha}\sqrt{\rho_{deb}}}\right) \tag{A3}$$

where $k_{deb} = 0.086$ is a material independent constant and ρ_{deb} is the debris dislocation density (Madec et al., 2003).

The total dislocation density is:

$$\rho_{tot}^{s} = \rho_{for}^{s} + \rho_{rev}^{s^{+}} + \rho_{rev}^{s^{-}}, \tag{A4}$$

where ρ_{for}^{s} is the forward dislocation density and $\rho_{rev}^{s^{+}}$ and $\rho_{rev}^{s^{-}}$ are the reversible dislocation densities associated with the s^{+} and s^{-}directions, respectively. Appropriate evolution laws are adopted for evolution of dislocation densities with shear strain and shearing direction (Khadyko et al., 2016; Kitayama et al., 2013; Kocks and Mecking, 1981):

(If $d\gamma^{s^{+}} > 0$)

$$\frac{\partial \rho_{for}^{s}}{\partial \gamma^{s}} = (1-p)k_{1}^{\alpha}\sqrt{\sum_{s'} g^{ss'}\rho_{tot}^{s'}} - k_{2}^{\alpha}(\dot{\varepsilon}, T)\rho_{for}^{s}, \tag{A5a}$$

$$\frac{\partial \rho_{rev}^{s^{+}}}{\partial \gamma^{s}} = pk_{1}^{\alpha}\sqrt{\sum_{s'} g^{ss'}\rho_{tot}^{s'}} - k_{2}^{\alpha}(\dot{\varepsilon}, T)\rho_{rev}^{s^{+}}, \tag{A6a}$$

$$\frac{\partial \rho_{rev}^{s^{-}}}{\partial \gamma^{s}} = -k_{1}^{\alpha}\sqrt{\sum_{s'} g^{ss'}\rho_{tot}^{s'}}\left(\frac{\rho_{rev}^{s^{-}}}{\rho_{0}^{s}}\right)^{m}, \tag{A7a}$$

(If $d\gamma^{s^{-}} > 0$)

$$\frac{\partial \rho_{for}^{s}}{\partial \gamma^{s}} = (1-p)k_{1}^{\alpha}\sqrt{\sum_{s'} g^{ss'}\rho_{tot}^{s'}} - k_{2}^{\alpha}(\dot{\varepsilon}, T)\rho_{for}^{s}, \tag{A5b}$$

$$\frac{\partial \rho_{rev}^{s^{+}}}{\partial \gamma^{s}} = -k_{1}^{\alpha}\sqrt{\sum_{s'} g^{ss'}\rho_{tot}^{s'}}\left(\frac{\rho_{rev}^{s^{+}}}{\rho_{0}^{s}}\right)^{m}, \tag{A6b}$$

$$\frac{\partial \rho_{rev}^{s^{-}}}{\partial \gamma^{s}} = pk_{1}^{\alpha}\sqrt{\sum_{s'} g^{ss'}\rho_{tot}^{s'}} - k_{2}^{\alpha}(\dot{\varepsilon}, T)\rho_{rev}^{s^{-}}, \tag{A7b}$$

with the following initial conditions:

$$\rho_{for}^{s}(\gamma^{s} = 0) = 10^{11}\ m^{-2},\ \rho_{rev}^{s^{+}}(\gamma^{s} = 0) = 0\,\text{and}\,\rho_{rev}^{s^{-}}(\gamma^{s} = 0) = 0, \tag{A8}$$

where k_{1}^{α} is a coefficient controlling the rate of generation of statistically stored dislocations, k_{2}^{α} is a rate-sensitive coefficient for dynamic recovery (Beyerlein and Tomé, 2008), p is a reversibility parameter having a value between 0 and 1, and $g^{ss'}$ is an interaction matrix, m is a parameter accounting for the rate of dislocation recombination having value of 0.5 (Wen et al., 2015) and ρ_{0}^{s} is the total dislocation density at the moment of shear reversal on the sth slip system (Kitayama et al., 2013). Entries of the interaction matrix, $g^{ss'}$, describe the influence of dislocation density on the slip system s' on the accumulation of forest dislocations on the slip system s (Khadyko et al., 2016; Kocks et al., 1991; Teodosiu and Raphanel, 1991).

The rate-sensitive coefficient for dynamic recovery, k_{2}^{α}, is:

$$\frac{k_{2}^{\alpha}}{k_{1}^{\alpha}} = \frac{\chi b^{\alpha}}{g^{\alpha}}\left(1 - \frac{k_{B}T}{D^{\alpha}(b^{\alpha})^{3}}ln\left(\frac{\dot{\varepsilon}}{\dot{\varepsilon}_{0}}\right)\right), \tag{A9}$$

where, k_{B} is the Boltzmann constant, $\dot{\varepsilon}_{0} = 10^{7}$ is a reference strain rate, g^{α} is an effective activation enthalpy and D^{α} is a drag stress. The debris dislocation density is evolved with:

$$\frac{\partial \rho_{deb}}{\partial \gamma^{s}} = q^{\alpha} b^{\alpha}\sqrt{\rho_{deb}}\ k_{2}^{\alpha}(\dot{\varepsilon}, T)\rho_{tot}^{s}, \tag{A10}$$

where q^{α} is a dislocation recovery rate constant governing the amount of dislocations that get stored as debris, instead of being annihilated. Initial debris dislocation density is set to 0.1 m^{-2}.

In addition to dislocation-based evolution of slip resistance, a backstress on each slip system is introduced. The backstress was first implemented in EPSC in Wollmershauser et al. (2012). Here we use the same approach, while utilizing different backstress evolution laws. The present backstress evolution laws and the backstress implementation in EPSC are discussed in detail in Zecevic and Knezevic (2018), while here we only provide a brief description.

The backstress is introduced to EPSC by altering the loading conditions (4a) and (4b):

$$\boldsymbol{\sigma}^{c}\cdot\mathbf{m}^{s} - \tau_{bs}^{s} = \tau_{c}^{s}, \tag{A11}$$

$$\overset{\wedge}{\boldsymbol{\sigma}}^{c}\cdot\mathbf{m}^{s} - \dot{\tau}_{bs}^{s} = \dot{\tau}_{c}^{s}, \tag{A12}$$

where τ_{bs}^{s} is a backstress on a slip system. Analogues to Eq. (5), the backstress is assumed to evolve with shear rates:

$$\dot{\tau}_{bs}^{s} = \sum_{s^{'}} h_{bs}^{ss'}\dot{\gamma}^{s'}, \tag{A13}$$

where $h_{bs}^{ss'}$ is a backstress matrix. With introduction of the backstress the single crystal tangent stiffness retains the same form defined with Eq. (7), while the matrix $X^{ss'}$,entering the tangent stiffness, becomes:

$$X^{ss'} = h^{ss'} + h_{bs}^{ss'} + \mathbf{C}^{c}\cdot\mathbf{m}^{s}\otimes\ \mathbf{m}^{s'}. \tag{A14}$$

Before defining the backstress matrix, $h_{bs}^{ss'}$, evolution laws for the backstress on a slip system, τ_{bs}^{s}, are introduced:

$$\tau_{bs}^{s} = \mathbf{m}^{s}\cdot\boldsymbol{\sigma}_{bs}^{c} = \tau_{bs,sys}^{s} + 2\sum_{s^{'}}\mathbf{m}^{s}\cdot\mathbf{m}^{s'}\tau_{bs,sys*}^{s'}, \tag{A15}$$

with

$$\tau_{bs,sys*}^{s'} = \begin{cases} \tau_{bs,sys}^{s'}\ \mathit{if}\ \ \tau_{bs,sys}^{s'} > 0 \\ \ \ 0\ \mathit{if}\ \ \tau_{bs,sys}^{s'} < 0 \end{cases} \tag{A16}$$

where $\boldsymbol{\sigma}_{bs}^{c}$ is a backstress tensor formed by superimposing slip system sources of backstress, $\tau_{bs,sys}^{s'}$, and the sum over s' spans over all slip systems and $s' \neq s$.

The slip system source of backstress is evolved with:

(if $d\gamma^{s^{+}} > 0$ and $\tau_{bs,sys}^{s^{+}} > 0$)

$$\tau_{bs,sys}^{s^{+}} = \tau_{bs}^{sat}(1 - \exp(-\nu\gamma^{s^{+}})), \tag{A17}$$

$$\tau_{bs,sys}^{s^{-}} = -A\tau_{bs,sys}^{s^{+}}, \tag{A18}$$

(if $d\gamma^{s^{+}} > 0$ and $\tau_{bs,sys}^{s^{+}} < 0$)

$$\tau_{bs,sys}^{s^{+}} = -(A+1)\tau_{bs}^{sat}\exp\left(-\frac{\gamma^{s^{-}}}{\gamma_{b}}\right) + \tau_{bs}^{sat} \tag{A19}$$

$$\tau_{bs,sys}^{s^{-}} = -\frac{1}{A}\tau_{bs,sys}^{s^{+}} \tag{A20}$$

where τ_{bs}^{sat} is a saturation value for backstresses, A is a parameter for asymmetric evolution of backstress on a slip system in two different directions $s+$ and s-, γ_{b} and ν are material parameters. The shear strain γ^{s} is recorded from the point of local load reversal.

Since the slip resistance and the backstress are defined as functions of shear strain, the hardening matrix, $h^{ss'}$, and the backstress matrix, $h_{bs}^{ss'}$, can be defined as:

$$h^{ss'} = \frac{\partial\tau_{c}^{s}}{\partial\gamma^{s'}};\ \ h_{bs}^{ss'} = \frac{\partial\tau_{bs}^{s}}{\partial\gamma^{s'}}. \tag{A21}$$

The expressions for $h^{ss'}$ and $h_{bs}^{ss'}$ are provided in Zecevic and Knezevic (2018).

Introduction of realistic strength interaction coefficients, $L^{ss'}$, results in non-positive definiteness of hardening matrix, $h^{ss'}$ (Zecevic and Knezevic, 2018), meaning that the necessary condition for determination of shear rates on active slip systems is not fulfilled (Hill, 1966). Therefore, issues in the solution procedure show up both at the single crystal and polycrystal level. To treat the major issue, which is loss of ellipticity of the polycrystal tangent stiffness, a diagonalization procedure is proposed in Zecevic and Knezevic (2018). The procedure involves correction of hardening matrix, $h^{ss'}$, before evaluating the single crystal tangent stiffness with Eqs. (7) and (A14). It is assumed that the single crystal problem is solved, i.e. shear rates on active slip systems are known. The corrected hardening matrix, h_{d}^{ss}, is diagonal, ensuring positive definiteness:

$$h_{d}^{ss} = \frac{1}{\Delta\gamma^{s}}\sum_{s^{'}} h^{ss'}\Delta\gamma^{s'} \tag{A22}$$

where $\Delta\gamma^{s'}$ are calculated increments in shear strain on active slip systems, while indices s and s' go over active slip systems.

References

Abaqus, 2012. Abaqus Analysis User's Manual. Dassault Systèmes, Providence, RI, USA.

Al-Harbi, H.F., Knezevic, M., Kalidindi, S.R., 2010. Spectral approaches for the fast computation of yield surfaces and first-order plastic property closures for polycrystalline materials with cubic-triclinic textures. CMC Comput. Mater. Continua 15, 153–172.

Anand, L., 2004. Single-crystal elasto-viscoplasticity: application to texture evolution in polycrystalline metals at large strains. Comput. Methods Appl. Mech. Eng. 193, 5359–5383.

Anand, L., Kothari, M., 1996. A computational procedure for rate-independent crystal plasticity. J. Mech. Phys. Solids 44, 525–558.

Ardeljan, M., Beyerlein, I.J., Knezevic, M., 2014. A dislocation density based crystal plasticity finite element model: application to a two-phase polycrystalline HCP/BCC composites. J. Mech. Phys. Solids 66, 16–31.

Ardeljan, M., Beyerlein, I.J., Knezevic, M., 2017. Effect of dislocation density-twin interactions on twin growth in AZ31 as revealed by explicit crystal plasticity finite element modeling. Int. J. Plast. 99, 81–101.

Ardeljan, M., Beyerlein, I.J., McWilliams, B.A., Knezevic, M., 2016a. Strain rate and temperature sensitive multi-level crystal plasticity model for large plastic deformation behavior: application to AZ31 magnesium alloy. Int. J. Plast. 83, 90–109.

Ardeljan, M., Knezevic, M., 2018. Explicit modeling of double twinning in AZ31 using crystal plasticity finite elements for predicting the mechanical fields for twin variant selection and fracture analyses. Acta. Mater. 157, 339–354.

Ardeljan, M., Knezevic, M., Nizolek, T., Beyerlein, I.J., Mara, N.A., Pollock, T.M., 2015. A study of microstructure-driven strain localizations in two-phase polycrystalline HCP/BCC composites using a multi-scale model. Int. J. Plast. 74, 35–57.

Ardeljan, M., Savage, D.J., Kumar, A., Beyerlein, I.J., Knezevic, M., 2016b. The plasticity of highly oriented nano-layered Zr/Nb composites. Acta. Mater. 115, 189–203.

Barrett, T.J., Savage, D.J., Ardeljan, M., Knezevic, M., 2018. An automated procedure for geometry creation and finite element mesh generation: application to explicit grain structure models and machining distortion. Comput. Mater. Sci. 141, 269–281.

Bauschinger, J., 1886. Über die Veränderung der Elasticitätsgrenze und Festigkeit des Eisen und Stahls durch Strecken und Quetschen, durch Erwarmen und Abkühlen und durch oftmal wiederholte Beanspruchung. In: Mitteilungen aus dem mechanisch-technischen Laboratorium der k. polytechnischen Schule, pp. 1877 -1836.

Ben Bettaieb, M., Débordes, O., Dogui, A., Duchêne, L., Keller, C., 2012. On the numerical integration of rate independent single crystal behavior at large strain. Int. J. Plast. 32–33, 184–217.

Beyerlein, I.J., Tomé, C.N., 2008. A dislocation-based constitutive law for pure Zr including temperature effects. Int. J. Plast. 24 (, 5), 867–895.

Borja, R.I., Wren, J.R., 1993. Discrete micromechanics of elastoplastic crystals. Int. J. Num. Meth. Engn. 36, 3815–3840.

Cheng, J., Shen, J., Mishra, R.K., Ghosh, S., 2018. Discrete twin evolution in Mg alloys using a novel crystal plasticity finite element model. Acta. Mater. 149, 142–153.

Eghtesad, A., Barrett, T.J., Germaschewski, K., Lebensohn, R.A., McCabe, R.J., Knezevic, M., 2018a. OpenMP and MPI implementations of an elasto-viscoplastic fast Fourier transform-based micromechanical solver for fast crystal plasticity modeling. Adv. Eng. Softw. 126, 46–60.

Eghtesad, A., Barrett, T.J., Knezevic, M., 2018b. Compact reconstruction of orientation distributions using generalized spherical harmonics to advance large-scale crystal plasticity modeling: verification using cubic, hexagonal, and orthorhombic polycrystals. Acta. Mater. 155, 418–432.

Eghtesad, A., Zecevic, M., Lebensohn, R.A., McCabe, R.J., Knezevic, M., 2018c. Spectral database constitutive representation within a spectral micromechanical solver for computationally efficient polycrystal plasticity modelling. Comput. Mech. 61 (, 1–2), 89–104.

Franciosi, P., Zaoui, A., 1982. Multislip in f.c.c. crystals a theoretical approach compared with experimental data. Acta Metall. 30, 1627–1637.

Ghorbanpour, S., Zecevic, M., Kumar, A., Jahedi, M., Bicknell, J., Jorgensen, L., Beyerlein, I.J., Knezevic, M., 2017. A crystal plasticity model incorporating the effects of precipitates in superalloys: application to tensile, compressive, and cyclic deformation of Inconel 718. Int. J. Plast. 99, 162–185.

Greenbaum, A., Chartier, T.P., 2012. Numerical Methods: Design, Analysis, and Computer Implementation of Algorithms. Princeton University Press, Princeton, NJ.

Gribbin, S., Bicknell, J., Jorgensen, L., Tsukrov, I., Knezevic, M., 2016. Low cycle fatigue behavior of direct metal laser sintered Inconel alloy 718. Int. J. Fatigue 93, 156–167 Part 1.

Hasegawa, T., Yakou, T., Karashima, S., 1975. Deformation behaviour and dislocation structures upon stress reversal in polycrystalline aluminium. Mater. Sci. Eng. 20, 267–276.

Hill, R., 1966. Generalized constitutive relations for incremental deformation of metal crystals by multislip. J. Mech. Phys. Solids 14 (, 2), 95–102.

Horstemeyer, M.F., Potirniche, G.P., Marin, E.B., 2005. Crystal plasticity. Handbook of Materials Modeling. Springer.

Hosford, W.F., Caddell, R.M., 2011. Metal Forming: Mechanics and Metallurgy. Cambridge University Press, New York, USA.

Hutchinson, J., 1970. Elastic-plastic behaviour of polycrystalline metals and composites. Proc. R. Soc. London. A. Math. Phys. Sci. 319, 247–272.

Jahedi, M., Ardeljan, M., Beyerlein, I.J., Paydar, M.H., Knezevic, M., 2015. Enhancement of orientation gradients during simple shear deformation by application of simple compression. J. Appl. Phys. 117.

Jahedi, M., Paydar, M.H., Zheng, S., Beyerlein, I.J., Knezevic, M., 2014. Texture evolution and enhanced grain refinement under high-pressure-double-torsion. Mater. Sci. Eng. A 611, 29–36.

Kalidindi, S.R., Bronkhorst, C.A., Anand, L., 1992. Crystallographic texture evolution in bulk deformation processing of FCC metals. J. Mech. Phys. Solids 40 (, 3), 537–569.

Kalidindi, S.R., Duvvuru, H.K., Knezevic, M., 2006. Spectral calibration of crystal plasticity models. Acta. Mater. 54, 1795–1804.

Khadyko, M., Dumoulin, S., Cailletaud, G., Hopperstad, O.S., 2016. Latent hardening and plastic anisotropy evolution in AA6060 aluminium alloy. Int. J. Plast. 76, 51–74.

Kitayama, K., Tomé, C.N., Rauch, E.F., Gracio, J.J., Barlat, F., 2013. A crystallographic dislocation model for describing hardening of polycrystals during strain path changes. Application to low carbon steels. Int. J. Plast. 46, 54–69.

Knezevic, M., Al-Harbi, H.F., Kalidindi, S.R., 2009. Crystal plasticity simulations using discrete Fourier transforms. Acta. Mater. 57 (, 6), 1777–1784.

Knezevic, M., Beyerlein, I.J., Brown, D.W., Sisneros, T.A., Tomé, C.N., 2013a. A polycrystal plasticity model for predicting mechanical response and texture evolution during strain-path changes: application to beryllium. Int. J. Plast. 49, 185–198.

Knezevic, M., Beyerlein, I.J., Lovato, M.L., Tomé, C.N., Richards, A.W., McCabe, R.J., 2014a. A strain-rate and temperature dependent constitutive model for BCC metals incorporating non-Schmid effects: application to tantalum–tungsten alloys. Int. J. Plast. 62, 93–104.

Knezevic, M., Capolungo, L., Tomé, C.N., Lebensohn, R.A., Alexander, D.J., Mihaila, B., McCabe, R.J., 2012. Anisotropic stress-strain response and microstructure evolution of textured α-uranium. Acta. Mater. 60, 702–715.

Knezevic, M., Carpenter, J.S., Lovato, M.L., McCabe, R.J., 2014b. Deformation behavior of the cobalt-based superalloy Haynes 25: experimental characterization and crystal plasticity modeling. Acta. Mater. 63, 162–168.

Knezevic, M., Crapps, J., Beyerlein, I.J., Coughlin, D.R., Clarke, K.D., McCabe, R.J., 2016a. Anisotropic modeling of structural components using embedded crystal plasticity constructive laws within finite elements. Int. J. Mech. Sci. 105, 227–238.

Knezevic, M., Drach, B., Ardeljan, M., Beyerlein, I.J., 2014c. Three dimensional predictions of grain scale plasticity and grain boundaries using crystal plasticity finite element models. Comput. Methods Appl. Mech. Eng. 277, 239–259.

Knezevic, M., Kalidindi, S.R., Fullwood, D., 2008a. Computationally efficient database and spectral interpolation for fully plastic Taylor-type crystal plasticity calculations of face-centered cubic polycrystals. Int. J. Plast. 24 (, 7), 1264–1276.

Knezevic, M., Kalidindi, S.R., Mishra, R.K., 2008b. Delineation of first-order closures for plastic properties requiring explicit consideration of strain hardening and crystallographic texture evolution. Int. J. Plast. 24 (, 2), 327–342.

Knezevic, M., Landry, N.W., 2015. Procedures for reducing large datasets of crystal orientations using generalized spherical harmonics. Mech. Mater. 88, 73–86.

Knezevic, M., McCabe, R.J., Lebensohn, R.A., Tomé, C.N., Liu, C., Lovato, M.L., Mihaila, B., 2013b. Integration of self-consistent polycrystal plasticity with dislocation density based hardening laws within an implicit finite element framework: application to low-symmetry metals. J. Mech. Phys. Solids 61 (, 10), 2034–2046.

Knezevic, M., Savage, D.J., 2014. A high-performance computational framework for fast crystal plasticity simulations. Comput. Mater. Sci. 83, 101–106.

Knezevic, M., Zecevic, M., Beyerlein, I.J., Bingert, J.F., McCabe, R.J., 2015. Strain rate and temperature effects on the selection of primary and secondary slip and twinning systems in HCP Zr. Acta Mater. 88, 55–73.

Knezevic, M., Zecevic, M., Beyerlein, I.J., Lebensohn, R.A., 2016b. A numerical procedure enabling accurate descriptions of strain rate-sensitive flow of polycrystals within crystal visco-plasticity theory. Comput. Methods Appl. Mech. Eng. 308, 468–482.

Knockaert, R., Chastel, Y., Massoni, E., 2000. Rate-independent crystalline and polycrystalline plasticity, application to FCC materials. Int. J. Plast. 16, 179–198.

Kocks, U.F., Brown, T.J., 1966. Latent hardening in aluminum. Acta Metall. 14, 87–98.

Kocks, U.F., Franciosi, P., Kawai, M., 1991. A forest model of latent hardening and its application to polycrystal deformations. Textures Microstruct. 14, 1103–1114.

Kocks, U.F., Mecking, H., 1981. Kinetics of flow and strain-hardening. Acta Metall. 29, 1865–1875.

Kocks, U.F., Tomé, C.N., Wenk, H.-R., 1998. Texture and Anisotropy. Cambridge University Press.

Lebensohn, R.A., Kanjarla, A.K., Eisenlohr, P., 2012. An elasto-viscoplastic formulation based on fast Fourier transforms for the prediction of micromechanical fields in polycrystalline materials. Int. J. Plast. 32–33, 59–69.

Lebensohn, R.A., Tomé, C.N., 1993. A self-consistent anisotropic approach for the simulation of plastic deformation and texture development of polycrystals: application to zirconium alloys. Acta Metall. Mater. 41, 2611–2624.

Lebensohn, R.A., Zecevic, M., Knezevic, M., McCabe, R.J., 2016. Average intragranular misorientation trends in polycrystalline materials predicted by a viscoplastic self-consistent approach. Acta. Mater. 104, 228–236.

Li, L., Shen, L., Proust, G., 2014. A texture-based representative volume element crystal plasticity model for predicting Bauschinger effect during cyclic loading. Mater. Sci. Eng. A 608, 174–183.

Lipinski, P., Berveiller, M., 1989. Elastoplasticity of micro-inhomogeneous metals at large strains. Int. J. Plast. 5, 149–172.

Madec, R., Devincre, B., Kubin, L., Hoc, T., Rodney, D., 2003. The role of collinear interaction in dislocation-induced hardening. Science 301, 1879–1882.

Mánik, T., Holmedal, B., 2014. Review of the Taylor ambiguity and the relationship between rate-independent and rate-dependent full-constraints Taylor models. Int. J. Plast. 55, 152–181.

Nagtegaal, J.C., Veldpaus, F.E., 1984. On the implementation of finite strain plasticity equations in a numerical model. Numer. Methods Ind. Form. Processes 351–371.

Neil, C.J., Wollmershauser, J.A., Clausen, B., Tomé, C.N., Agnew, S.R., 2010. Modeling lattice strain evolution at finite strains and experimental verification for copper and stainless steel using in situ neutron diffraction. Int. J. Plast. 26, 1772–1791.

Nugmanov, D., Knezevic, M., Zecevic, M., Sitdikov, O., Markushev, M., Beyerlein, I.J., 2018. Origin of plastic anisotropy in (ultra)-fine-grained Mg–Zn–Zr alloy processed by isothermal multi-step forging and rolling: experiments and modeling. Mater. Sci. Eng. A 713, 81–93.

Pavlina, E.J., Lee, M.-G., Barlat, F., 2015. Observations on the nonlinear unloading behavior of advanced high strength steels. Metall. Mater. Trans. A 46, 18–22.

Peirce, D., Asaro, R.J., Needleman, A., 1982. An analysis of nonuniform and localized deformation in ductile single crystals. Acta Metall. Mater. 30, 1087–1119.

Poulin, C.M., Korkolis, Y.P., Kinsey, B.L., Knezevic, M., 2019. Over five-times improved elongation-to-fracture of dual-phase 1180 steel by continuous-bending-under-tension. Mater. Des. 161, 95–105.

Roemer, T.J., Barrett, T.J., Knezevic, M., Kinsey, B.L., Korkolis, Y.P., 2019. Experimental study of continuous-bending-under-tension of AA6022-T4. J. Mater. Process. Technol. 266, 707–714.

Savage, D.J., Beyerlein, I.J., Knezevic, M., 2017. Coupled texture and non-Schmid effects on yield surfaces of body-centered cubic polycrystals predicted by a crystal plasticity finite element approach. Int. J. Solids Struct. 109, 22–32.

Savage, D.J., Knezevic, M., 2015. Computer implementations of iterative and non-iterative crystal plasticity solvers on high performance graphics hardware. Comput. Mech. 56, 677–690.

Schröder, J., Miehe, C., 1997. Aspects of computational rate-independent crystal plasticity. Comput. Mater. Sci 9, 168–176.

Segurado, J., Lebensohn, R.A., Llorca, J., Tomé, C.N., 2012. Multiscale modeling of plasticity based on embedding the viscoplastic self-consistent formulation in implicit finite elements. Int. J. Plast. 28, 124–140.

Simo, J.C., Taylor, R.L., 1985. Consistent tangent operators for rate-independent elastoplasticity. Comput. Methods Appl. Mech. Eng. 48, 101–118.

Suli, E., Mayers, D., 2003. An Introduction to Numerical Analysis. Cambridge University Press.

Taylor, G.I., 1938. Plastic strain in metals. J. Inst. Metals 62, 307–324.

Teodosiu, C., Raphanel, J.L., 1991. Finite element simulations of large elastoplastic deformations of multicrystals. In: Proceedings of the International Seminar MECAMAT91, pp. 153–168.

Turner, P.A., Tomé, C.N., 1994. A study of residual stresses in Zircaloy-2 with rod texture. Acta Metall. Mater. 42, 4143–4153.

Van Houtte, P., 1982. On the equivalence of the relaxed Taylor theory and the Bishop-Hill theory for partially constrained plastic deformation of crystals. Mater. Sci. Eng. 55, 69–77.

van Mier, J.G.M., 1997. Fracture Procseses of Concrete. CRC Press, USA.

Veluri, S.P., Roy, C.J., Luke, E.A., 2012. Comprehensive code verification techniques for finite volume CFD codes. Comput. Fluids 70, 59–72.

Wagoner, R.H., Lim, H., Lee, M.-G., 2013. Advanced Issues in springback. Int. J. Plast. 45, 3–20.

Wen, W., Borodachenkova, M., Tomé, C.N., Vincze, G., Rauch, E.F., Barlat, F., Grácio, J.J., 2015. Mechanical behavior of Mg subjected to strain path changes: experiments and modeling. Int. J. Plast. 73, 171–183.

Wollmershauser, J.A., Clausen, B., Agnew, S.R., 2012. A slip system-based kinematic hardening model application to in situ neutron diffraction of cyclic deformation of austenitic stainless steel. Int. J. Fatigue 36, 181–193.

Wu, P.D., MacEwen, S.R., Lloyd, D.J., Jain, M., Tugcu, P., Neale, K.W., 2005. On pre-straining and the evolution of material anisotropy in sheet metals. Int. J. Plasticity 21, 723–739.

Zang, S.-l., Lee, M.-g., Hoon Kim, J., 2013. Evaluating the significance of hardening behavior and unloading modulus under strain reversal in sheet springback prediction. Int. J. Mech. Sci. 77, 194–204.

Zecevic, M., Beyerlein, I.J., Knezevic, M., 2017. Coupling elasto-plastic self-consistent crystal plasticity and implicit finite elements: applications to compression, cyclic tension-compression, and bending to large strains. Int. J. Plast. 93, 187–211.

Zecevic, M., Beyerlein, I.J., McCabe, R.J., McWilliams, B.A., Knezevic, M., 2016a. Transitioning rate sensitivities across multiple length scales: microstructure-property relationships in the Taylor cylinder impact test on zirconium. Int. J. Plast. 84, 138–159.

Zecevic, M., Knezevic, M., 2015. A dislocation density based elasto-plastic self-consistent model for the prediction of cyclic deformation: application to AA6022-T4. Int. J. Plast. 72, 200–217.

Zecevic, M., Knezevic, M., 2017. Modeling of Sheet Metal Forming Based on Implicit Embedding of the Elasto-Plastic Self-Consistent Formulation in Shell Elements: application to Cup Drawing of AA6022-T4. JOM 1–8.

Zecevic, M., Knezevic, M., 2018. Latent hardening within the elasto-plastic self-consistent polycrystal homogenization to enable the prediction of anisotropy of AA6022-T4 sheets. Int. J. Plast. 105, 141–163.

Zecevic, M., Knezevic, M., Beyerlein, I.J., Tomé, C.N., 2015a. An elasto-plastic self-consistent model with hardening based on dislocation density, twinning and de-twinning: application to strain path changes in HCP metals. Mater. Sci. Eng. A 638, 262–274.

Zecevic, M., Korkolis, Y.P., Kuwabara, T., Knezevic, M., 2016b. Dual-phase steel sheets under cyclic tension–compression to large strains: experiments and crystal plasticity modeling. J. Mech. Phys. Solids 96, 65–87.

Zecevic, M., Lebensohn, R.A., McCabe, R.J., Knezevic, M., 2019a. Modelling recrystallization textures driven by intragranular fluctuations implemented in the viscoplastic self-consistent formulation. Acta. Mater. 164, 530–546.

Zecevic, M., McCabe, R.J., Knezevic, M., 2015b. A new implementation of the spectral crystal plasticity framework in implicit finite elements. Mech. Mater. 84, 114–126.

Zecevic, M., Roemer, T., Knezevic, M., Korkolis, Y., Kinsey, B., 2016c. Residual Ductility and Microstructural Evolution in Continuous-Bending-under-Tension of AA-6022-T4. Materials 9, 130.

Zecevic, M., Upadhyay, M.V., Polatidis, E., Panzner, T., Van Swygenhoven, H., Knezevic, M., 2019b. A crystallographic extension to the Olson-Cohen model for predicting strain path dependence of martensitic transformation. Acta. Mater. 166, 386–401.

Zeng, T., Shao, J.F., Xu, W.Y., 2015. A micromechanical model for the elastic–plastic behavior of porous rocks. Comput. Geotech. 70, 130–137.